Habilitation work

Membrane at the nanoscale – molecular insights by fluorescence microscopy

by

Radek Šachl

Content

1. Introduction

Biophysical experiments performed in the last decades have shown that nanoscale organization of lipids and proteins in cellular membranes is rather complicated and far from being completely random.[1–3] On the contrary, many lipids and membrane proteins spontaneously co-cluster and oligomerize into larger functional units, which may be essential for proper functioning of biological membranes[2]. To give a few examples for all, gangliosides self-assemble in plasma membranes into several tens of nanometre large lipid nanodomains, forming a platform for ligand to receptor interactions (**Chapter 5.1.4**).[4,5] Similarly, protein FGF2 (Fibroblast Growth Factor 2), involved in wound healing, cell proliferation or tumour induced angiogenesis,[6,7] oligomerizes in the plasma membrane into functional hexa- to octamers.[8] These oligomers are thought to be essential for opening of trans-membrane pores and successful translocation of FGF2 into the extracellular space, where the protein fulfils its various functions (**Chapter 5.2**). Or, interestingly, coiled-coil interactions between SNARE proteins (soluble N-ethyl-maleimide-sensitive factor attachment protein receptors) essentially mediate intra-cellular events of membrane fusion in eukaryotic cells (**Chapter 5.3**).[9] The fusion itself is crucial for a variety of cellular functions, including controlled release of neurotransmitters, fertilization, communication or material exchange in eukaryotic cells, but it can also be used in *in vivo* applications for the delivery of DNA material into cells.[10,11]

All these findings were made possible by the rapid development of advanced biophysical approaches that can detect and characterize nanoscopic objects in the membrane by offering high spatial and temporal resolution. These high-resolution approaches include advanced fluorescence microscopy and spectroscopy techniques,[3,12–14] but also label-free techniques (such as recently developed Interferometric SCATtering microscopy (iSCAT),[15,16] or 'standard' techniques comprising x-ray, neutron scattering, electron or atomic force microscopy and others[2]). Despite of this rapid technological development, biophysical characterization of the plasma membrane at the nanoscale is extremely challenging, on the one hand due to its inherent complexity and dynamic nature and on the other hand due to the complexity of advanced biophysical approaches that allow for the characterization of biological membranes at such detail. Consequently, nanoscale organization of biological membranes as well as the processes taking place in them are far away from being understood.

2. Focus of the thesis

This habilitation work focuses primarily on the development of two advanced fluorescence methods: MC-FRET (Förster Resonance energy Transfer analysed by Monte-Carlo simulations) and dual(+1)-FCS (Fluorescence Correlation Spectroscopy) and their applications in studies of the organisation of the membrane at the nanoscale and the interactions of proteins with the membrane.

The first method, MC-FRET (explained in **Chapter 5.1.1** to **Chapter 5.1.3** and attached papers **PAPER II, III** and **VIII**), has been developed with the goal to improve the lacking lateral and trans-bilayer resolution of the approaches based on fluorescence microscopy, which severely limits the detection and detailed characterization of subwavelength lipid nanodomains recently discovered in the plasma membranes of living cells.[2] Over the years, we have been upgrading and applying the method, which now can detect membrane nanodomains as small as a few nanometres, and, importantly, determine their size and surface density (**Chapter 5.1.3** and **Chapter 5.1.4** and **PAPER I**, **PAPERs IV-VII**). Thanks to the excellent trans-bilayer resolution, the MC-FRET can also characterize inter-leaflet organization of the nanodomains, i.e. it can distinguish inter-leaflet coupled (= registered) from inter-leaflet independent or anti-registered nanodomains (**Chapter 5.1.5 and PAPER VIII** and **IX**). Considering the extremely thin thickness of the lipid bilayer, the resolution of currently available microscopical approaches are insufficient for such purposes.

The second fluorescence microscopy approach, dual(+1)-FCS (**Chapter 5.2 and PAPER XI**), was introduced in 2020 and represents a new statistical single molecule and single vesicle assay that determines the brightness of individually diffusing in-membrane oligomers and correlates their oligomerization state with membrane pore formation. In this way, in-membrane oligomerization of proteins can be linked directly to the formation of membrane pores in one experiment under physiological conditions (**PAPER XII**). Considering that up to now, membrane permeabilization and in-membrane protein/peptide oligomerisation were processes that have been studied in separate biophysical or biochemical experiments, this technique opens new possibilities in the research of membrane pore formation, a process that is tightly related to cellular apoptosis or the action of many antibiotics.

In the recent years, we have used these methods together with other advanced fluorescence spectroscopy and microscopy approaches in studies of nanoscale organisation of lipid bilayers as well as protein-membrane interactions that result in the reorganisation of the membrane. More specifically, by using MC-FRET we showed that model lipid bilayers consisting of more than two

distinct types of lipids may be, similarly to the plasma membranes of living cells, heterogeneous at the nanoscale, containing nanometre sized heterogeneities, called throughout the thesis lipid nanodomains (**PAPER I**). We demonstrated that these nanodomains are extremely dynamic but long-lived and have features significantly differing from the micro-sized phase-separated domains, that had been frequently used as mimics of plasma membrane nanoheterogeneities (**PAPER I**). Moreover, using the same technique, we were able to explain the molecular basis for the segregation of gangliosides, which form an important class of receptor lipids found in the outer plasma membrane leaflet, into small nanoscopic platforms (**PAPER IV** and **PAPER V**) and showed that binding of Cholera toxin to these platforms induces their nanoscale reorganization and significantly changes their intrinsic properties (**PAPER VI** and **PAPER VII**).

In **Chapter 5.2**, we have employed dual(+1)-FCS to investigate membrane translocation of FGF2, which, based on our previous research, is accompanied by membrane pore formation. We showed that FGF2 oligomers with about 7 to 8 subunits represent the functional entities of productive membrane insertion that permeabilize the membrane whereas larger oligomers are products of non-functional oligomerisation of FGF2 (**PAPER XI and PAPER XII**). Of note, we could also monitore the oligomeric state of FGF2 on the same lipid vesicle over time, which allowed for the detection of sudden increases in the FGF2 oligomeric state that were accompanied by increased membrane permeability. In this way, in-membrane oligomerization of FGF2 was linked directly to the formation of membrane pores.

Finally, the last chapter of the thesis (**Chapter 5.3** and **PAPER XIII** and **PAPER XIV**) summarises our research focused on two synthetic mimics of fusogenic proteins based on two complementary lipopeptides that can induce membrane fusion both in vivo and in vitro. In our work, we elucidated the molecular mechanism by which the lipopeptides induce the initial steps of membrane fusion and highlight the importance of both lipopeptides in the fusogenic mechanism that has a strong potential to be used successfully in vivo for the delivery of genetical material into cells.

Thank you for your attention to this work.
Radek Šachl, in Prague 3.6.2021

3. Plasma membrane models

The plasma membrane of living cells represents a greatly complex and dynamic system. It can be approximated by two parallel sheets consisting of mainly lipids, proteins, ions, and of course water.[1,17] To reduce the complexity of this system, scientists have invented several synthetic models for these membranes, including free-standing membranes represented by vesicles and membranes prepared on a solid support, hereafter called Supported Phospholipid Bilayers (SPBs, **Figure 3.1**).

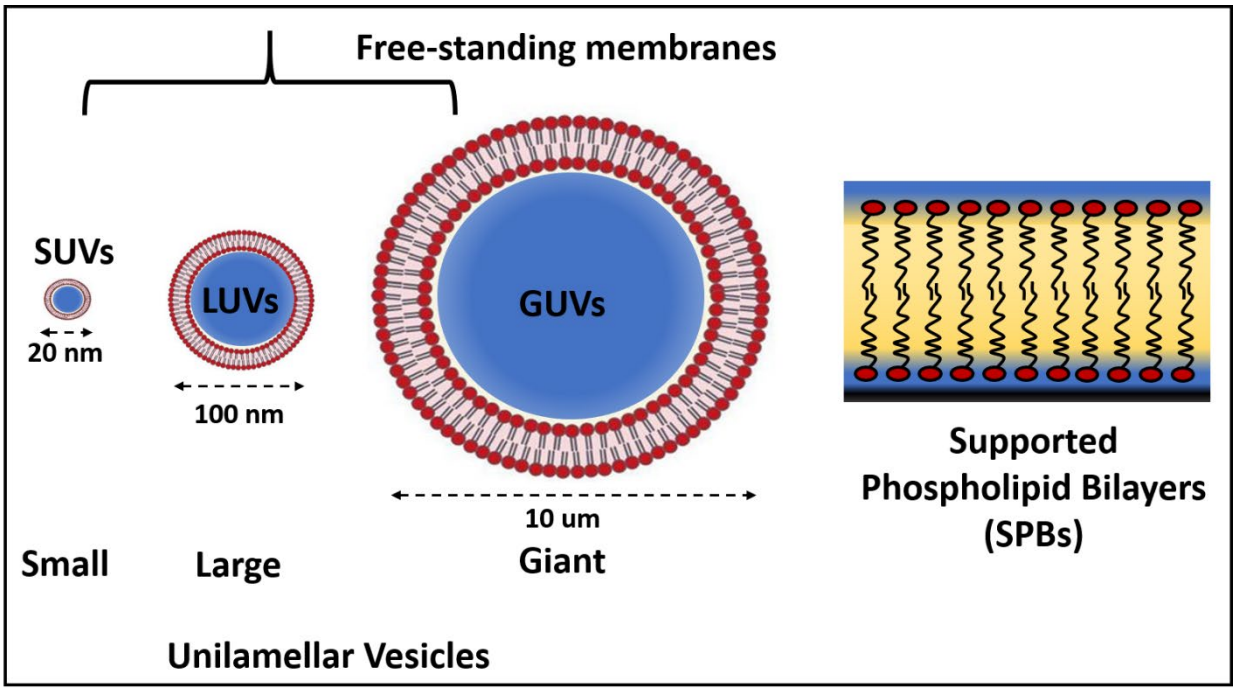

Figure 3.1: Classification of plasma membrane models into free-standing membrane models represented by SUVs, LUVs and GUVs, and Supported Phospholipid Bilayers (SBPs).

Depending on their size, vesicles can be divided into small (SUVs, having a diameter of ca 20 nm), large (LUVs, having a diameter of ca 100 nm) and giant unilamellar vesicles (GUVs, having a diameter of ca 10 μm).[18] SUVs (prepared by sonication of the hydrated lipid film) are extremely small and consist of a highly curved lipid bilayer. In contrast, LUVs (prepared by extrusion of the hydrated film through polycarbonate filters with a defined pore size) are large enough to be considered as objects containing a flat lipid bilayer. Both SUVs and LUVs diffuse freely in the solution as small solute molecule do. This behavior distinguishes them markedly from GUVs,

which, due to their significantly higher mass, incline to settle down on the microscopy glass. GUVs can be up to two orders of magnitude larger than LUVs, and thus resemble living cells in their size. They can be immobilized on the microscopy glass and imaged individually by means of a fluorescence microscope. Alternatively, fluorescence measurements can be performed at specific places of the GUV membrane, allowing for a detailed biophysical analysis of the GUV membrane.

SPBs (routinely prepared by calcium induced vesicle fusion on glass) are in direct contact with the solid support.[19] This makes them an ideal system to be investigated by super-resolution microscopy, whose use is limited to the area in the closest proximity of the solid support.[8,20,21] At the same time, SPBs are less ideal for the studies of transmembrane proteins that protrude from the membrane. Such proteins may get into contact with the solid support, which, in an extreme case can make the proteins fully immobile, or at least partially impeded.[22] Such negative effect of the support is unwanted and can be partially eliminated by tethering or cushioning the bilayers.[23,24] These attempts, however, have not always been successful and usually require an extensive modification of the membrane support.[25,26]

4. Methods

4.1 Fluorescence spectroscopy and microscopy

In the last decades, biophysical approaches based on fluorescence spectroscopy and microscopy have become extremely popular in membrane biophysics and have been thoroughly reviewed elsewhere.[27–29] They enable to study biological membranes close to or at physiological conditions while offering a high nanometer resolution in space and nanosecond resolution in time. Furthermore, thanks to the great advances in organic chemistry and molecular biology, specific components of lipid membranes, including individual lipids or transmembrane proteins, can nowadays be fluorescently labeled, which allows for observing only the molecules of interest with negligible contribution of the surrounding. This makes fluorescent approaches the methods of choice when cellular membranes are studied.

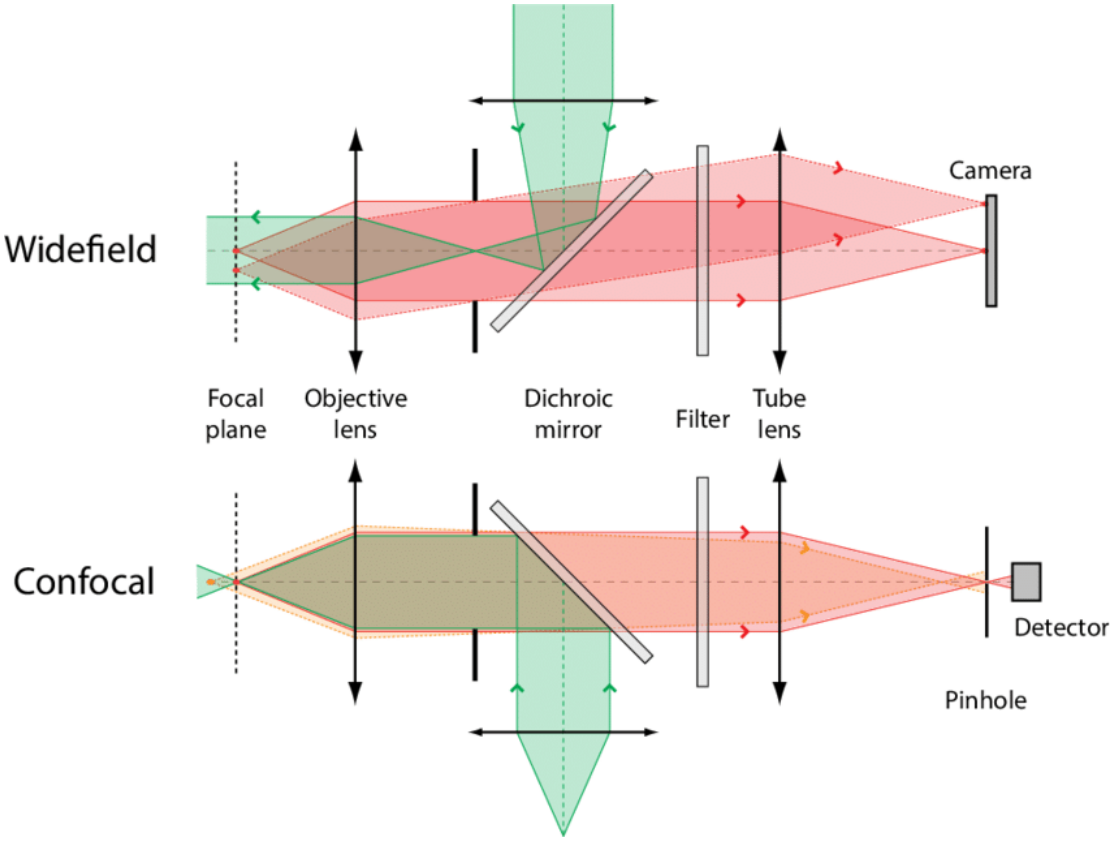

Figure 4.1: Schematic illustration of a widefield and confocal microscopes (the image taken from the dissertation RESOLFT nanoscopy with water-soluble synthetic fluorophores by Philipp J. Alt, Göttingen 2017)

A typical fluorescent microscope consists of several laser light sources, wavelength selective excitation and emission filters, an objective lens, mirrors and one or more detectors.[30] The specimen, placed into the focal plane of the objective, is illuminated by the light focused by the objective lens. The red-shifted emission is collected through the same objective and separated from the excitation light by a dichroic mirror (**Figure 4.1**). The light is further cleaned by an emission filter and focused on the detector plane by a tube lens. In principle, two different types of fluorescent microscopes can be distinguished: a widefield or confocal microscope, respectively.

In a widefield microscope, an area with the diameter of several micrometers is illuminated and imaged onto a CCD camera. Consequently, neighboring spots that are located within the illuminated area are imaged simultaneously. Despite the rapid technological development, the best up to date cameras can acquire an image consisting from a limited number of pixels with the framerate of only 1 ms, which significantly constraints the research of fast dynamic processes. Furthermore, in this setup, the emission is collected not only from the focal plane but to some extent also from the out-of-focus planes, which reduces the image contrast when thick samples are imaged.

In a confocal microscope, instead of exciting a large area, the excitation light is focused into a diffraction limited spot by the objective lens (**Figure 4.1**). The emission is collected by the same objective and projected on a single-point detector with sub-nanosecond time resolution. This setup thus allows for studying fast processes, however, to acquire an image of a larger area the sample needs to be scanned point by point in both x and y directions. Since a pinhole is placed into the conjugate focal plane in front of the detector, the undesired out-of-focus light is blocked efficiently.

4.2 Förster Resonance Energy Transfer (FRET) in a lipid bilayer

Förster resonance energy transfer (FRET), described in detail for instance,[31] is a nonradiative transfer of the excitation energy from a fluorescent donor to an acceptor molecule. It is a consequence of long-range dipole-dipole interactions within a donor-acceptor pair. The quantum-mechanical description of the phenomenon was firstly given by Theodor Förster, who showed that the rate of energy transfer depends inversely on the sixth power of the distance between the donor and the acceptor.[32]

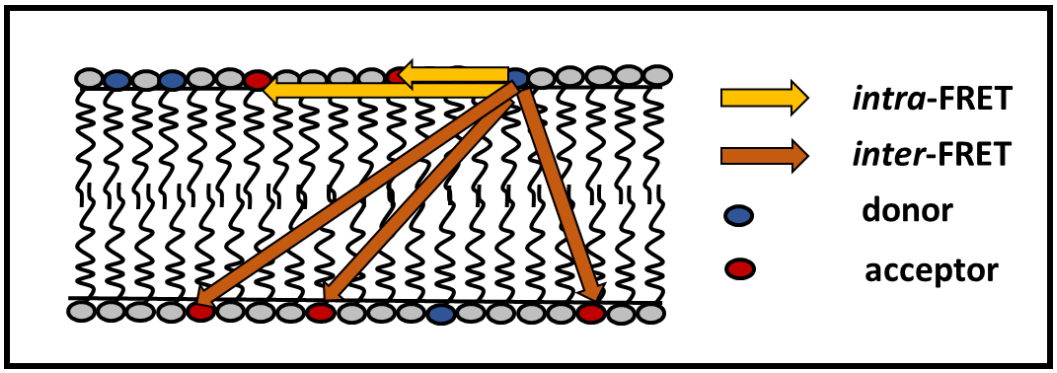

Figure 4.2: In a lipid bilayer approximated by two parallel sheets containing headgroup labelled fluorescent lipids, FRET will occur both within the same as well as between the two parallel leaflets. The excited state energy can be transferred to any of the nearby located acceptors, with the probability depending on the given donor-acceptor distance.

If a donor is surrounded by more than one acceptor, the excited state energy can be transferred to any of these acceptors with the probability depending on the distance between the given donor-acceptor pair. Such a situation arises when FRET occurs in a lipid bilayer between headgroup labelled donor and acceptor lipids (**Figure 4.2**). In this geometrical arrangement, FRET will happen both within one bilayer leaflet and between the two leaflets at the same time. Whereas the first process is referred to as *intra*-FRET and depends only on the surface concentration of acceptors, the latter one is known as *inter*-FRET and depends in addition on the distance between the two bilayer leaflets *d*. To express mathematically the kinetics of fluorescence deexcitation of the donors in the presence of acceptors, it is convenient to first introduce a so-called survival probability function $G(t)$ describing the probability that a donor is still found in the excited state at the time t after the excitation. This function is proportional to the donor fluorescence intensity $F_{\mathrm{D}}(t)$ when no FRET occurs and can be expressed as:[33]

$$G_{\mathrm{D}}(t) \approx F_{\mathrm{D}}(t) = \sum_i \alpha_i \, exp\left(-\frac{t}{\tau_i}\right). \qquad (4.1)$$

Here, $\alpha_i$denote the pre-exponential factors and $\tau_i$the corresponding fluorescence lifetimes, and $G_{\mathrm{D}}(t)$ the survival probability function in the absence of FRET. When several independent deexcitation processes occur at the same time, the total probability function $G_{\mathrm{TOT}}(t)$ equals the product of $G_{\mathrm{i}}(t)$ functions for individual deexcitation processes:

$$G_{\mathrm{TOT}}(t) = \prod G_i(t). \qquad (4.2)$$

By assuming dynamic limit conditions, where movements of dipoles are much faster than an energy transfer event, Bauman and Fayer showed that $G(t)$ for *intra*-FRET, G_{intra},[33] equals

$$ln\, G_{\text{intra}}(t) = -C_2\Gamma\left(\frac{2}{3}\right)\left(\frac{t}{\langle\tau\rangle}\right)^{1/3}, \quad (4.3)$$

Here, Γ denotes the gamma function, $\langle\tau\rangle$ the average fluorescence lifetime of donors in the absence of acceptors and C_2 the reduced surface concentration of acceptors. This concentration represents the average number of acceptors within the area of πR_0^2 and is related to the acceptor surface concentration C by: $C_2 = \pi R_0^2 C$. In the same work, the authors derived $G(t)$ for *inter*-FRET, $G_{\text{inter}}(t)$,[33]

$$ln\, G_{\text{inter}}(t) = -\frac{C_2}{3}\left(\frac{d}{R_0}\right)^2\left(\frac{2\mu}{3}\right)^{1/3}\int_0^{2/3\mu}(1-e^{-s})s^{-4/3}ds, \quad (4.4)$$

where θ_r is the angle between the bilayer normal and the vector connecting the locations of the donor and acceptor dipoles, $\mu = 3t\left(\frac{R_0}{d}\right)^6\frac{1}{2\langle\tau\rangle}$ and $s = 2\mu\cos^6\frac{\theta_r}{3}$. As a result, the kinetics of fluorescence deexcitation of the donors in the presence of acceptors, $F_{\text{DA}}(t)$, can be expressed for the classical case where both donors and acceptors are localized in the lipid bilayer at the same distance from the lipid-water interface as

$$F_{\text{DA}}(t) = G_{\text{intra}}(t)G_{\text{inter}}(t)F_{\text{D}}(t). \quad (4.5)$$

Fitting time-resolved fluorescence data by this equation enables to transversely localize fluorescent probes with sub-nanometre resolution and to accurately determine the surface concentration of acceptors.[34]

4.3 Fluorescence Correlation Spectroscopy (FCS) in a lipid bilayer

Fluorescence correlation spectroscopy, described in detail elsewhere [35–37], is a method based on the measurement of fluorescence fluctuations, which arise as individual fluorescent emitters diffuse in and out of a tiny (about 1 femtoliter large) excitation volume (**Figure 4.3A**). Correlation of the intensity signal at the time t, $I(t)$ and at the time τ later yields an autocorrelation function $G(\tau)$:

$$G(\tau) = \frac{\langle I(t)I(t+\tau)\rangle}{\langle I(t)\rangle^2} - 1 \quad . \quad (4.6)$$

$G(\tau)$ contains information about the number of fluorescent molecules in the confocal spot N and their corresponding diffusion time τ_{D}. τ_{D} stands for the average time it takes a molecule to diffuse from the center of the confocal spot (with the radius ω_0) to its boundary and is related to

the particle diffusion coefficient D by $D = \frac{\omega_0^2}{4\tau_D}$. In the case of a 2D diffusion in a planar lipid bilayer, the autocorrelation function can be expressed as[38]

$$G(\tau) = \frac{1}{N}\frac{1}{1+\frac{\tau}{\tau_D}}. \quad (4.7)$$

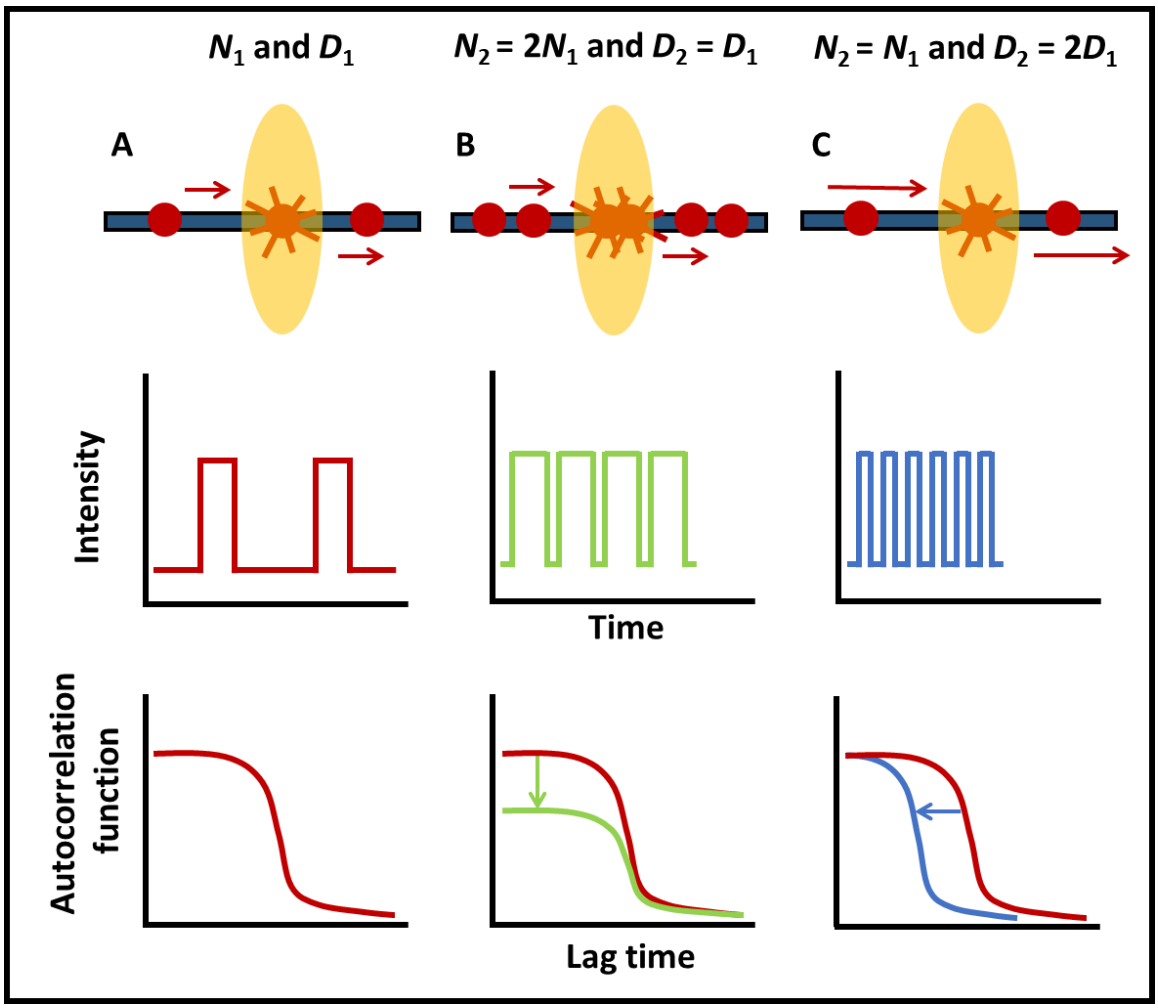

Figure 4.3: FCS measurement performed in a lipid bilayer. (A) Diffusion of fluorescent molecules across the confocal volume (in orange) focused on the lipid bilayer (in dark blue) will cause fluctuations in the fluorescence signal (middle row) and result in the autocorrelation function $G(\tau)$ with a positive amplitude $G(0)$ (bottom row). (B) Increase in the number of diffusing particles is accompanied by the decrease in $G(0)$. (C) Similarly, increase in the diffusion coefficient D is accompanied by shift of the whole $G(\tau)$ function to shorter lag times.

Increasing the number of fluorescent particles in the confocal volume will increase the amount of fluctuations while maintaining their period and will result in the decrease in the autocorrelation amplitude $G(0)$ (**Figure 4.3B**). It can be shown that an average of 1 fluorescent particle per confocal volume yields the best signal-to-noise ratio. Similarly, increasing the rate of diffusion in the membrane will reduce the period of observed fluctuations and result in a shift of the autocorrelation curve to shorter lag times τ (**Figure 4.3C**).

5. Results

5.1 Membrane Lipid Nanodomains (**PAPER I**)

Lipid bilayers formed by a single phospholipid are homogeneous in terms of their chemical composition. In contrast, bilayers containing more than one type of the phospholipids may separate into distinct coexisting phases differing in their physicochemical properties.[18] As shown on the classical ternary dioleoylphosphatidylcholine (DOPC)/Cholesterol (Chol)/sphingomyelin (SM) phase-diagram (**Figure 5.1**),[39,40] depending on the molar DOPC/Chol/SM ratio, the GUV bilayer may phase-separate into microscopic liquid-ordered (L_o) regions that are in coexistence with the surrounding liquid-disordered (L_d) phase or gel regions surrounded by the L_d phase. Moreover, as we showed in [3], the membrane of GUVs that appears homogeneous at the microscale may be heterogenous at the nanoscale, containing nanometer-sized domains, known as lipid nanodomains. By developing a new high-resolution technique MC-FRET, described in detail in **Chapter 5.2** and **Chapter 5.3**, we could characterize these entities (**Table 5.1**). They have sizes of about 10 nm in radius and occupy a significant fraction of the bilayer surface (up to 55%). In DOPC/SM (90/10) bilayers, the nanodomains contained in average 94 SM and 390 DOPC molecules.[3] These numbers yield a SM to DOPC molar ratio of 1:4. In DOPC/Chol/SM (65/25/10) bilayers, the nanodomains are estimated to contain 228 DOPC, 195 Chol and 78 SM molecules. This yields a 1:3 SM to DOPC ratio and a 1:2.5 SM to Chol ratio.[3] Thus, the number of DOPC molecules (which make the bilayer fluid) by far exceeds the number of SM molecules in the nanodomains. Thus, these considerations point to an L_d and not L_o character of the nanodomains that is typical for microscopically sized domains.

Although there is probably no major driving force responsible for nanodomain formation, the following factors may facilitate the nanoscopic segregation of sphingolipids: First, geometrical factors result in different packing preferences of DOPC and SM. Consequently, SM tends to be surrounded by other SM rather than DOPC molecules. Second, it has been documented by a variety of experimental approaches that SM and Chol preferably interact with each other (for a review see[41]) and that Chol promotes segregation of different PC components at low Chol contents whereas it suppresses the segregation at higher concentrations (above 50 mol%)[42]. Third, all these interactions are re-enforced by hydrogen bonding between –NH group of SM and hydroxyl group of Chol and between SM and DOPC[41,43–45]. And finally, temporal thermal fluctuations and fluctuations in concentration are most likely also involved[4647]. Thus, hypothetically, it is possible

that these temporal fluctuations function as seeds for the liquid disordered nanodomains in a similar way as nanodomains work as formation platforms for microscopic L_o phase domains.

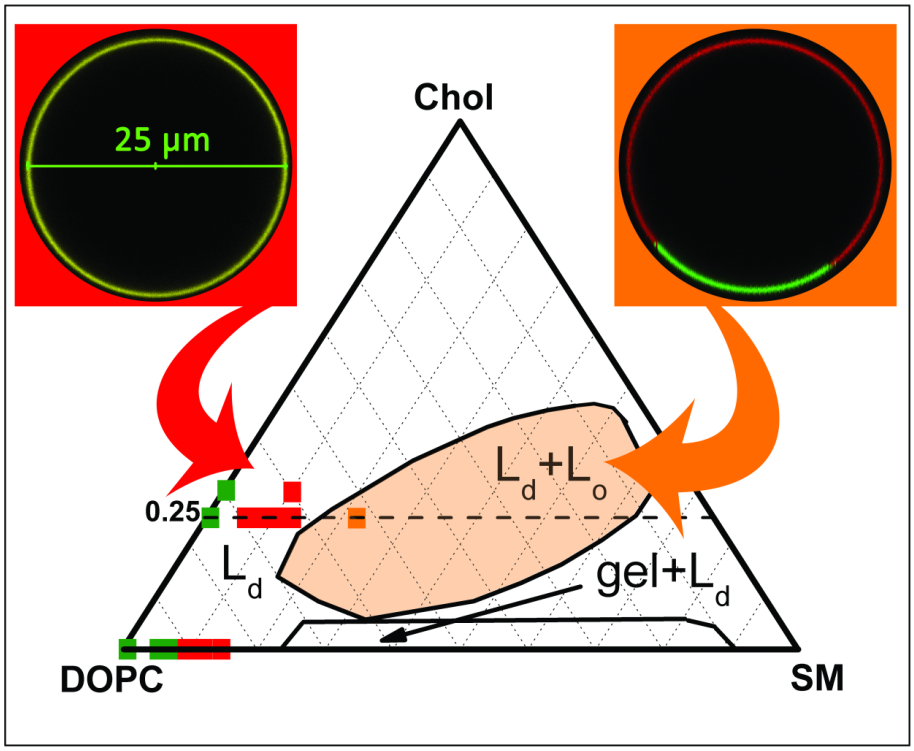

Figure 5.1 The DOPC/Chol/SM ternary phase diagram taken from [3]. The boundaries for the L_d/L_o and gel/L_d regions of phase coexistence were described in [39,40]. Selected points mark the compositions for which homogeneous bilayers (green squares), bilayers with liquid-disordered (L_d) nanodomains (red squares) or with microscopic liquid-ordered (L_o) phase domains (orange square) were found. The fluorescent microscopy images at the top show the apparent homogeneous nature of the bilayers containing nanodomains and the microscopic heterogeneity of mixtures in the L_d/L_o phase coexistence region. The figure was taken from [3].

Table 5.1. Average radius and area coverage of the nanodomains in DOPC/SM and DOPC/Chol/SM mixtures.

DOPC (mol%)	SM (mol%)	Chol (mol%)	Domain radius (nm)	Domain area (%)
100, 75, 70	0	0, 25, 30	Homogeneous distrib.	
95, 92	5, 8	0	Homogeneous distrib.	
90, 88, 85	10, 12, 15	0	8 ± 1 12 ± 3	37 ± 10 55 ± 10
95, 92, 90, 88	5, 8, 10, 12	0	Homogeneous distrib.	
70, 67, 65	5, 8, 10	25	9 ± 1	45 ± 5
63	12	25	Homogeneous distrib.	
70, 67	5, 8	25	Homogeneous distrib.	
65, 63	10, 12	25	8 ± 1	55 ± 5
60	10	30	9 ± 1	45 ± 5

5.1.1 Development of MC-FRET for the characterization of lipid nanodomains (PAPER II)

The spatial resolution of a fluorescence microscope is severely limited by the diffraction phenomena occurring at the objective, making it technically challenging to resolve structures with only tens of nanometers in diameter. This has motivated us to develop a new spectroscopic technique, called MC-FRET (FRET analyzed by Monte-Carlo simulations) that enables characterization of lipid nanodomains close to or even below 10 nm in radius.

FRET between a single donor and single acceptor has been often used in biophysics as a spectroscopic ruler for the measurements of intra-protein distances of several nanometers.[29] We have used the same phenomenon for the measurements of nanodomain sizes in lipid bilayers. The first attempts in this direction have been made by M. Prieto et al.[48] The approach is based on the fact that formation of nanodomain structures forces a homogeneous distribution of donors and acceptors (**Figure 5.2A**) into a heterogeneous one (**Figure 5.2B-D**). Depending on the affinity of the donors and acceptors to the nanodomains (characterized by the distribution constant of the donors, $K_{\mathrm{D}}(\mathrm{D})$, and acceptors, $K_{\mathrm{D}}(\mathrm{A})$, as $K_D(\mathrm{D/A}) = [\mathrm{D/A\ inside}]/[\mathrm{D/A\ outisde}]$) the following situations may arise: Case 0): $K_{\mathrm{D}}(\mathrm{D}) = 1$ and $K_{\mathrm{D}}(\mathrm{A}) = 1$. Consequently, the probes are distributed homogenously across the entire lipid bilayer regardless of the presence of nanodomains (**Figure 5.2A**). Such a situation does not allow for the detection of nanodomains using MC-FRET. Case I) $K_{\mathrm{D}}(\mathrm{D}) > 1$ and $K_{\mathrm{D}}(\mathrm{A}) > 1$, implying that both donors and acceptors accumulate inside of the

nanodomains (**Figure 5.2B**). Such a spatial accumulation of the probes decreases the average distance between the donors and acceptors and leads to enhanced FRET and faster relaxation of the donors into the ground state (**Figure 5.2E**) as compared to the homogeneous probe distribution (Case 0, **Figure 5.2A**). In this and the following cases, the FRET efficiency as well as the shape

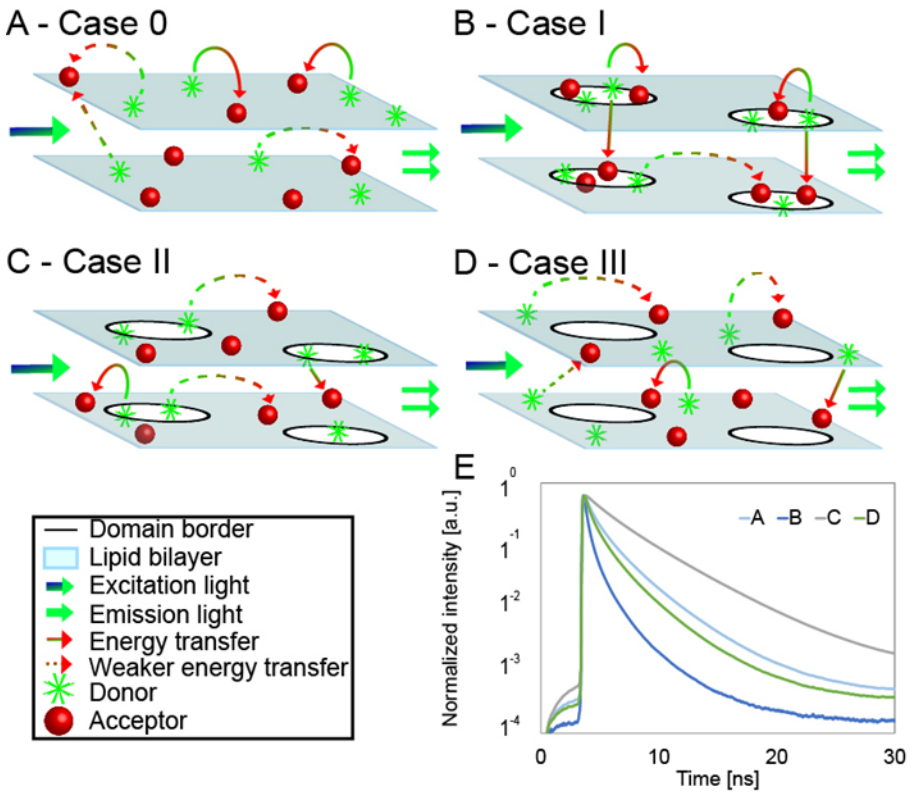

Figure 5.2 (A-D) Possible arrangements of the donors and acceptors in respect to the nanodomains and (E) the implications of the given distributions for the time-resolved decays of the donors in the presence of acceptors. (A) A nanoscopically homogeneous bilayer with randomly distributed donors and acceptors; A nanoscopically heterogenous bilayer with (B) both the donors and acceptors exhibiting high affinity to the nanodomains; (C) donors localized in the nanodomains and acceptors excluded from the nanodomains and (D) both the donors and acceptors excluded from the nanodomains. The figure was taken from [49].

of time-resolved fluorescence decays of the donors in the presence of acceptors is influenced by the size, concentration and inter-leaflet organization of the nanodomains, i.e. the parameters that can be determined by MC-FRET. Case II) $K_D(D) > 1$ and $K_D(A) < 1$ or $K_D(D) < 1$ and $K_D(A) >$

1, which results in the accumulation of donors and acceptors in distinct bilayer regions, and consequently spatial separation of the donors from the acceptors (**Figure 5.2C**). Such a probe distribution yields a lower FRET efficiency and slower relaxation kinetics in comparison to Case 0 (**Figure 5.2E**). And finally, case III) $K_{\mathrm{D}}(\mathrm{D}) < 1$ and $K_{\mathrm{D}}(\mathrm{A}) < 1$. Since both donors and acceptors are excluded from the nanodomains in this case, the efficiency of FRET will be increased, and the relaxation kinetics accelerated in comparison to homogenous probe distribution.

5.1.2 Work-flow of MC-FRET

The MC-FRET analysis is based on fitting experimental time-resolved fluorescence decays of the donors in the presence of acceptors by the decays generated by MC simulations and follows the basic scheme depicted on **Figure 5.3**. The entire procedure starts by generation of a defined number of nanodomains on the bilayer surface. The nanodomains are assumed to be circular in shape and uniform in size, and are characterized by the nanodomain radius, $\langle R \rangle$, and their surface density, $\langle A \rangle$. In the next step, the donors and acceptors are distributed between the nanodomains and the remaining bilayer part according to their K_{D} (D) and K_{D} (A). The total number of acceptors that enters the simulation is estimated on the same sample prior to nanodomain formation by FRET (see also **Chapter 4.2**). Then, a donor is randomly excited, and the time at which energy transfer takes place calculated. This process is modulated by the overall energy transfer rate Ω_{i} according to $\Delta t_i = -ln\gamma/\Omega_i$, where γ is a randomly generated number between 0-1. The outcome of each simulation step is the time interval Δt_i between the excitation and energy transfer event. By constructing a histogram of Δt_i intervals, the total survival probability function $G(t)$ is obtained, and the simulated decay of the donors quenched by the acceptors $F_{\mathrm{DA}}(t)$ calculated $F_{\mathrm{DA}}(t) = G(t)F_{\mathrm{D}}(t)$. The simulated decay is fitted to the experimental one by varying the input simulation parameters, *i.e.,* the domain radius $\langle R \rangle$, the area fraction occupied by the domains $\langle A \rangle$, and $K_D(\mathrm{D/A})$ (**Figure 5.3**).

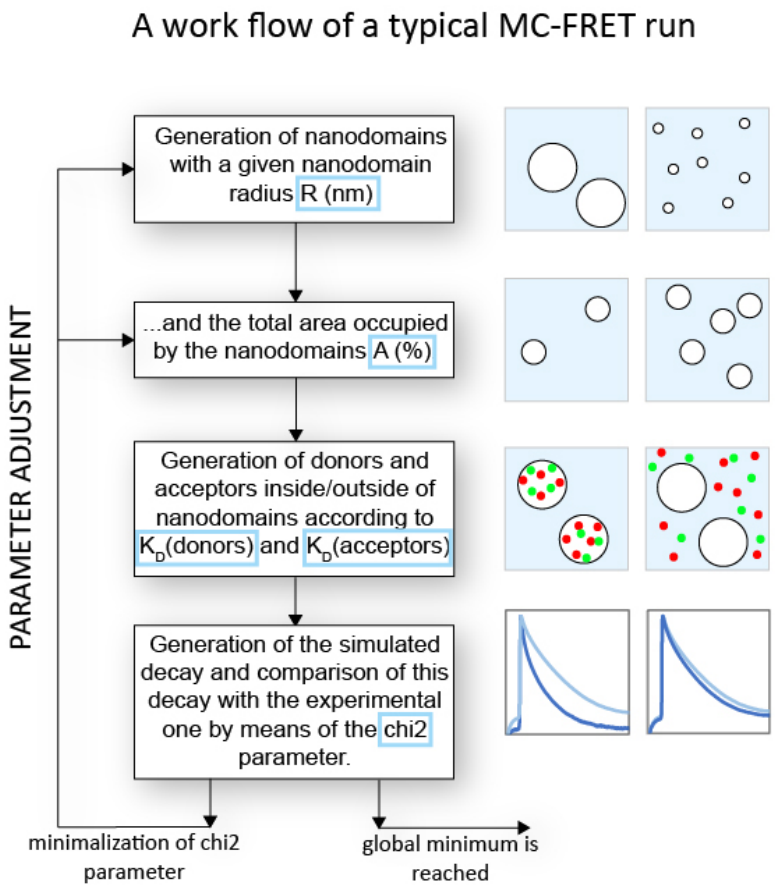

Figure 5.3 A workflow of an MC-FRET simulation yielding the optimized nanodomain radius, the total area occupied by the nanodomains and optionally the distribution constants K_D(donors), K_D(acceptors). The figure was taken from [49].

5.1.3 What nanodomain sizes can be resolved by MC-FRET? (PAPER III)

Nanodomains can be detected by MC-FRET only if their formation influences the efficiency of FRET that affects the shape of time-resolved fluorescence decays of the donors quenched by the acceptors. In the past, we have investigated the limitations of MC-FRET in detail and have shown that the resolution depends significantly on the affinity of the donors and acceptors to the nanodomains.[50,51] To characterize the resolution of MC-FRET, it is convenient to introduce a parameter *RES*, defined as

$$RES = \frac{\sum_{i=1}^{n} abs(F_{\mathrm{DA,homo}}(t_i) - F_{\mathrm{DA,hetero}}(t_i))}{F_{\mathrm{DA,homo}}(t_i) n} \cdot 100 \quad (5.1)$$

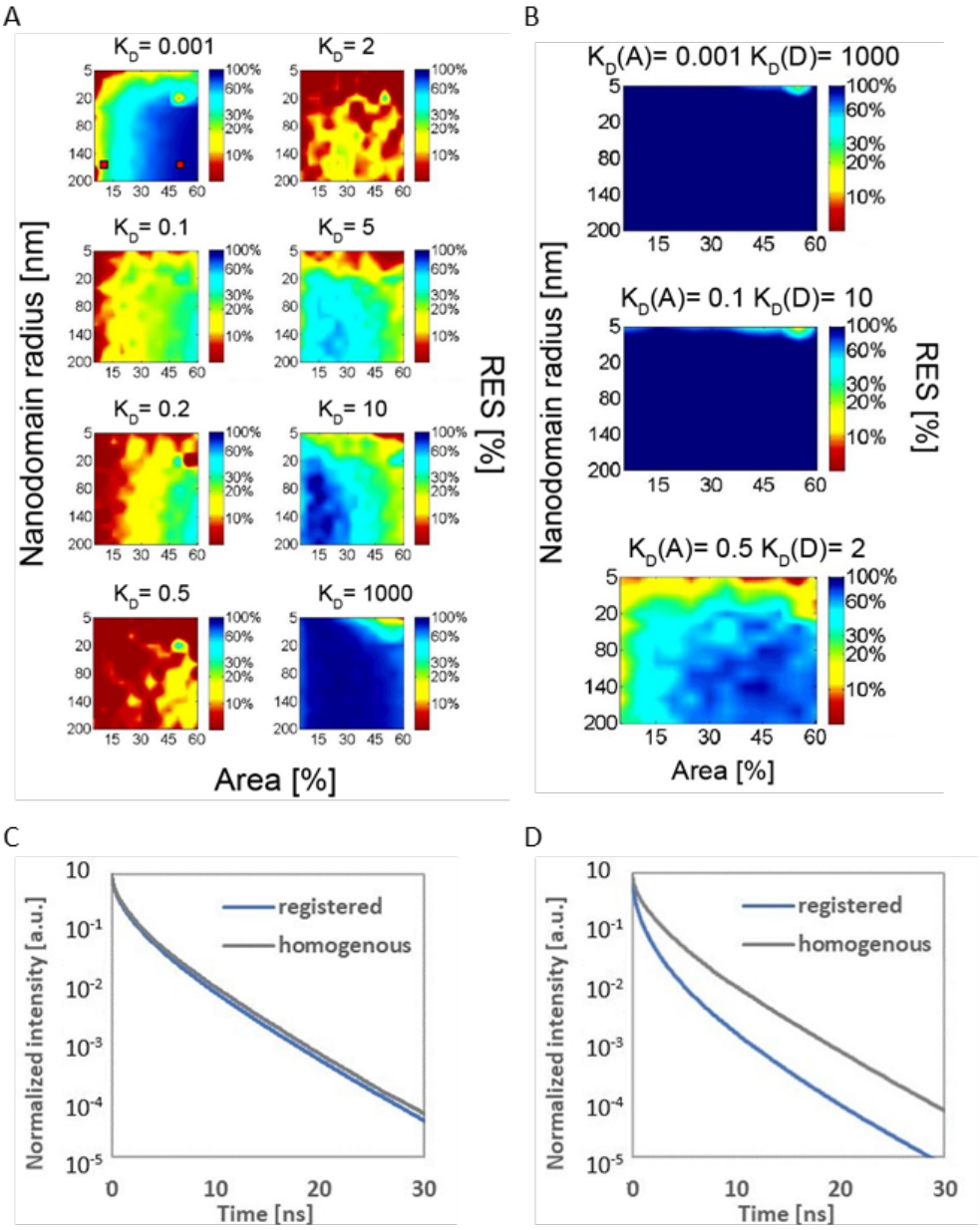

Figure 5.4 The resolution of MC-FRET in the detection of membrane nanodomains as a function of the nanodomain radius and the fractional area occupied by the nanodomains shown for various K_Ds. The resolution is characterized by the parameter *RES* defined in the text. (A) K_D (D) = K_D(A), (B) K_D (D) ≥ 1 and K_D (A) ≤ 1. (C-D) Time-resolved fluorescence decays for a homogeneous bilayer and the bilayer containing registered nanodomains characterized by *RES* = 19.5 % (C) and *RES* = 83.8 % (D). The decays were extracted from the positions in the resolution diagram depicted by solid red squares. The figure was taken from [49].

This parameter quantifies the difference between the time-resolved fluorescence decay recorded in the absence of nanodomains, $F_{\mathrm{DA,homo}}(t_i)$, where probes are distributed homogeneously, and the decay recorded in the presence of nanodomains, $F_{\mathrm{DA,hetero}}(t_i)$, where, in contrast, the donors and acceptors are distributed heterogeneously.

We have plotted this parameter as a function of the average nanodomain radius $\langle R \rangle$ and the fractional area occupied by the nanodomains $\langle A \rangle$ on **Figure 5.4** for Cases I, II and III (see **Chapter 5.1.1** for their definition)**.** On this Figure, *RES* can be interpreted in the following way: 1) $RES \leq 10\%$ (red colour on the colormap bar of **Figure 5.4**), yielding very similar decays for the homogeneous and heterogeneous probe distributions. At the same time, this parameter value corresponds to the change in the steady-state intensity of donors, $\langle F_{\mathrm{DA,hetero}} \rangle / \langle F_{\mathrm{DA,homo}} \rangle$, and the average fluorescence lifetime, $\langle \tau_{\mathrm{DA,hetero}} \rangle / \langle \tau_{\mathrm{DA,homo}} \rangle$, of less than 10 %. Such conditions are unfavourable for the MC-FRET analysis. 2) $RES \in (10; 20\rangle\%$ (yellow colour on the colormap bar of **Figure 5.4**), enabling the detection of nanodomains by MC-FRET. This parameter value is accompanied by the change in $\langle F_{\mathrm{DA,hetero}} \rangle / \langle F_{\mathrm{DA,homo}} \rangle$ by more than 10 % and the change in $\langle \tau_{\mathrm{DA,hetero}} \rangle / \langle \tau_{\mathrm{DA,homo}} \rangle$ that does not exceed 10 %. 3) $RES \in (20; 30\rangle\%$ (green colour on the colormap bar of **Figure 5.4**), yielding clearly distinct decays. This parameter value results in the change of $\langle F_{\mathrm{DA,hetero}} \rangle / \langle F_{\mathrm{DA,homo}} \rangle$ of up to 20 % and the change in $\langle \tau_{\mathrm{DA,hetero}} \rangle / \langle \tau_{\mathrm{DA,homo}} \rangle$ that is above 10 %. 4) $RES \in (30; 60\rangle\%$ (cyan colour on the colormap bar of **Figure 5.4**), leading to the change in $\langle F_{\mathrm{DA,hetero}} \rangle / \langle F_{\mathrm{DA,homo}} \rangle$ of up to 40 % and the change in $\langle \tau_{\mathrm{DA,hetero}} \rangle / \langle \tau_{\mathrm{DA,homo}} \rangle$ of more 10 %. 5) Finally, if $RES > 60\%$ (blue colour on the colormap bar of **Figure 5.4**), $\langle F_{\mathrm{DA,hetero}} \rangle / \langle F_{\mathrm{DA,homo}} \rangle > 30\%$ and $\langle \tau_{\mathrm{DA,hetero}} \rangle / \langle \tau_{\mathrm{DA,homo}} \rangle > 20\%$.

A careful inspection of the figure reveals that in case of a high probe affinity to either the nanodomains or the region outside of them (characterized by $K_{\mathrm{D}}(\mathrm{D/A}) = 1000$ or $K_{\mathrm{D}}(\mathrm{D/A}) = 1/1000$) the resolution of MC-FRET is excellent for most combinations of $\langle R \rangle$ and $\langle A \rangle$. To identify the Case that provides the best resolution, we generated the diagrams for $K_{\mathrm{D}}(\mathrm{D/A}) = 10$ or $K_{\mathrm{D}}(\mathrm{D/A}) = 1/10$, respectively (**Figure 5.4**). Based on this comparison, Case II ($K_{\mathrm{D}}(\mathrm{D}) > 1$ and $K_{\mathrm{D}}(\mathrm{A}) < 1$) performs the best, followed by Case I ($K_{\mathrm{D}}(\mathrm{D}) > 1$ and $K_{\mathrm{D}}(\mathrm{A}) > 1$), whereas Case III ($K_{\mathrm{D}}(\mathrm{D}) < 1$ and $K_{\mathrm{D}}(\mathrm{A}) < 1$) performs the worst. Most important of all, even such low and physically realistic $K_{\mathrm{D}}(\mathrm{D/A})$ values provide enough resolution for all cases.

In summary, this computational work shows that the resolution of MC-FRET is enough to detect and characterize nanometer-sized domains. Several years ago, these positive results opened in our lab the doors for the research of lipid nanodomains that can - even nowadays - be hardly detected by any other advanced physicochemical approach.

5.1.4 Nanoscale organization of gangliosides studied by MC-FRET (PAPER IV and PAPER V)

Gangliosides are glycosphingolipids consisting of a hydrophobic ceramide base and a hydrophilic sugar chain that contains at least one sialic acid residue (**Figure 5.5**)[52]. At first glance, they attract attention with their extremely bulky headgroup that both from the functional and structural point of view represents a crucial part of the molecule. The disproportionality between the headgroup and the hydrophobic backbone explains the propensity of gangliosides to self-assemble in aqueous solutions into micelles. More importantly, gangliosides associate within lipid membranes at low surface concentrations to form nanoscopic heterogeneities called ganglioside nanodomains that work as nanoscopic platforms for ligand to receptor interactions. Despite of the biological importance of gangliosides, the features of ganglioside nanodomains, as well as the molecular factors driving gangliosides to form nanoscopic heterogeneities in lipid bilayers are to a large extent unclear.

This motivated us to investigate self-assembly of gangliosides in lipid membranes in more detail. Over the years, these efforts have resulted in publication of several research papers and reviews.[2–4,53–57]

The predisposition of gangliosides to segregate and form nanodomains is prompt by their structure at three different levels: the hydrophobic tails, the water-lipid interface and the bulky sugar headgroups [58]. The influence of each of these structural features is discussed in the following sections.

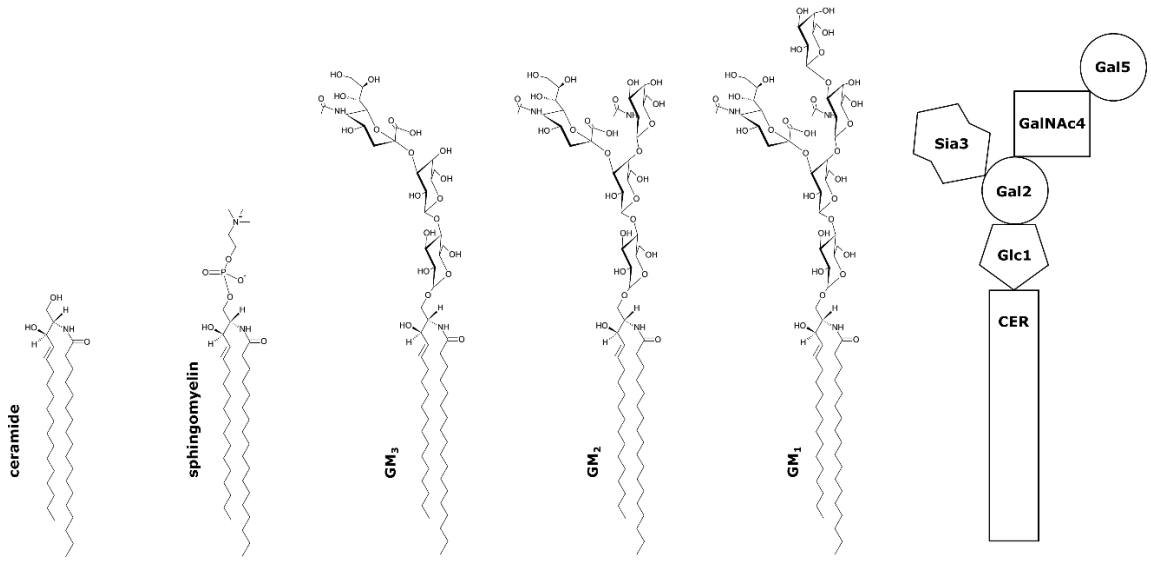

Figure 5.5 Chemical structures of the sphingolipids. From left to right: ceramide (CER), sphingomylein (SM) and monosialogangliosides GM_3, GM_2 and GM_1. The last panel is a cartoon depiction on GM_1 where the molecule is broken down into CER backbone and its sugar headgroup, with different sugar residues highlighted: glucose (Glc1), galactose (Gal2 and Gal5), sialic acid (SIAL3) and N-acetylgalactosamine (GalNAc4). The figure was taken from [56].

5.1.4.1 Impact of ganglioside's headgroup on the formation of nanodomains

The impact of ganglioside's headgroup on the formation of nanodomains can be approached by reducing the number of sugar units of the ganglioside oligosaccharide chain and investigating the ability of gangliosides to spontaneously self-organize into lipid nanodomains. In our recent work, we studied the effect of reducing the size of the headgroup from ganglioside GM_1, to ganglioside GM_2 and GM_3 and compared the aggregation behavior to the structurally related sphingomyelin. By combining a high-resolution technique MC-FRET (here used for the detection and characterization of ganglioside nanodomains with nanometer resolution) with atomistic molecular dynamic simulations, we identified the key factors that drive and impair segregation of gangliosides into nanodomains:

1) The ganglioside aggregation is mainly driven by their headgroups despite the negative charge of the sialic acid group they contain. As follows from **Table 5.2**, they are responsible for up to ~67% of the interaction energy between the gangliosides and promote the formation of a hydrogen bonding network that stabilizes the nanodomains.

Table 5.2. Pairwise interaction energies $|H^{norm}|$ between the ganglioside headgroup (HG), interface region (I) and acyl chains (AC), and the surrounding gangliosides (GM_i), SM, DOPC, and Chol (± standard errors of the mean) in the concentrated mode. Each pairwise interaction is normalized per the second lipid in the pair (listed in the row).

		Normalized Interaction Enthalpies $\|H^{norm}\|$ (kJ mol^{-1})							
		GM_i	**%**	**SM**	**%**	**DOPC**	**%**	**Chol**	**%**
GM_1	**HG**	-166.3 ± 2.9	66.9	-104.2 ± 0.8	48.8	-96.2 ± 1.8	56.8	-2.1 ± 0.1	5.0
	I	-20.8 ± 0.5		-5.7 ± 0.4	2.7	-3.1 ± 0.1	1.8	-0.8 ± 0.0	1.9
	AC	-61.5 ± 1.3	8.4 24.7	-103.8 ± 1.7	48.6	-69.9 ± 1.5	41.3	-39.0 ± 0.3	93.1
	Total	-248.6 ± 4.7	100.0	-213.7 ± 2.9	100.0	-169.3 ± 3.4	100.0	-41.9 ± 0.4	100
GM_2	**HG**	-134.1 ± 2.6	56.7	-99.4 ±0.5	50.4	-81.6 ± 1.0	50.5	-1.7 ± 0.1	4.3
	I	-25.7 ± 0.5		-5.4 ± 0.2	2.7	-3.3 ± 0.1	2.1	-0.5 ± 0.0	1.3
	AC	-76.7 ± 1.5	10.9 32.4	-92.6 ±1.4	46.9	-76.1 ± 2.2	47.3	-37.6 ± 0.7	94.5
	Total	-236.5 ± 4.6	100.0	-197.4 ± 2.1	100.0	-160.9 ± 3.3	100.0	-39.8 ± 0.8	100.0
GM_3	**HG**	-119.2 ± 3.0	65.2	-91.3 ± 1.1	54.3	-60.1 ± 1.3	44.7	-2.6 ± 0.1	6.1
	I	-4.6 ± 0.4		-3.3 ± 0.3	2.0	-3.1 ± 0.1	2.3	-0.6 ± 0.0	1.4
	AC	-59.1 ± 1.2	2.5 32.3	-89.8 ± 1.6	43.3	-60.5 ± 2.7	45.0	-39.3 ± 1.1	92.0
	Total	-182.9 ± 4.6	100.0	-184.4 ± 3.0	100.0	-123.7 ± 4.1	100.0	-42.5 ± 1.2	100

2) The size and structure of the ganglioside headgroup influences the mutual ganglioside interactions and the resulting nanodomain size (**Figure 5.6**). We identified the N-acetylgalactosamine sugar moiety in GM_2 as the group impairing the stability of ganglioside nanodomains through the disruption of hydrogen bonding of the neighbouring sugars. This is reflected in a broad size distribution of GM_2 nanodomains in comparison to GM_1 or GM_3 nanodomains.
3) The formation of nanodomains is accompanied by several conformational changes in the gangliosides. The most striking of all is the straightening of terminal sialic acid groups (**Figure 5.7**). Because this has little impact on the solvent exposure of these receptor groups, we conclude that the biological role of ganglioside nanodomains is not to expose the terminal sialic acid to the solvent but rather to provide a nanoscopic platform with elevated local

concentrations of ganglioside receptors.

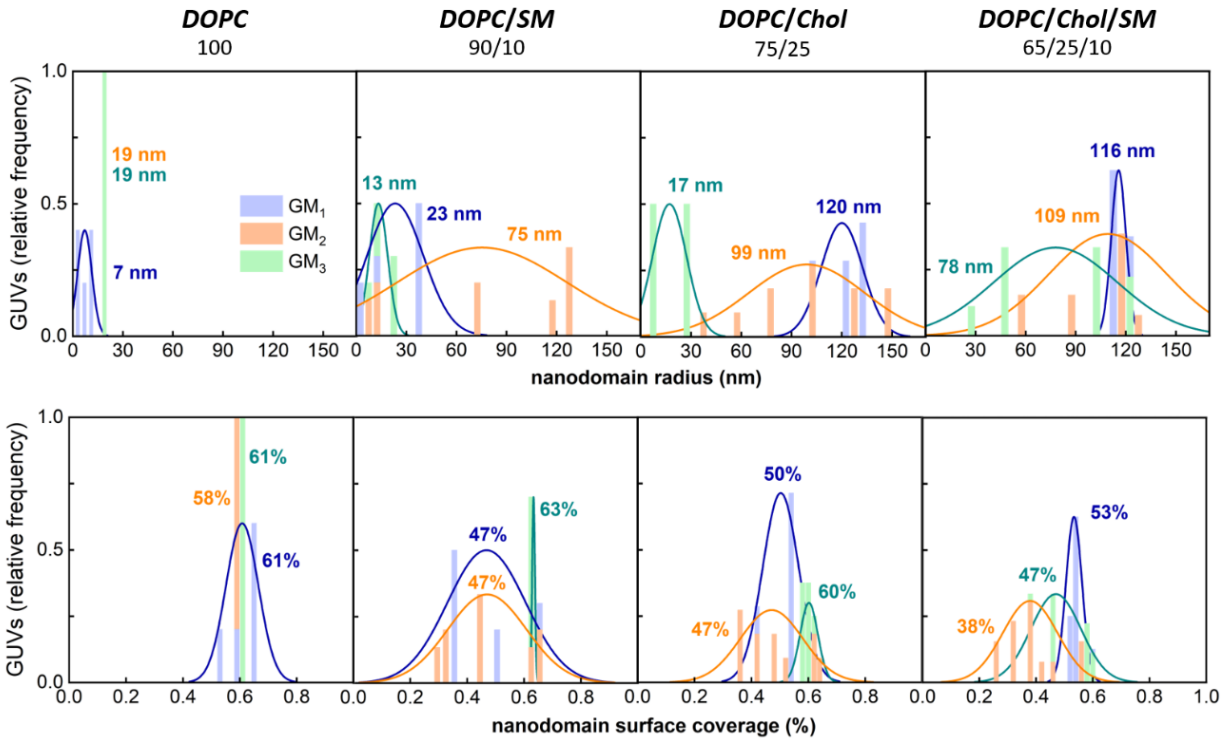

Figure 5.6 Characterization of the nanoscopic segregation of gangliosides in lipid bilayers of different lipid compositions. Both nanodomain size (top panel) and relative surface area coverage (bottom panel) distributions are shown for the bilayers containing 5 mol% GM_1 (blue), GM_2 (orange) or GM_3 (green). MC-FRET analysis has been performed for each imaged GUV individually. All distributions account for 5 to 15 GUVs, depending on the variability. The inset values refer to the average radius and average surface coverage of the corresponding distribution. The figure was taken from [56].

4) Despite being called ganglioside nanodomains, they are in fact majorly composed of the surrounding bulk lipids including sphingomyelin and cholesterol, with gangliosides being only a minor component of the nanodomains (**Table 5.3**).

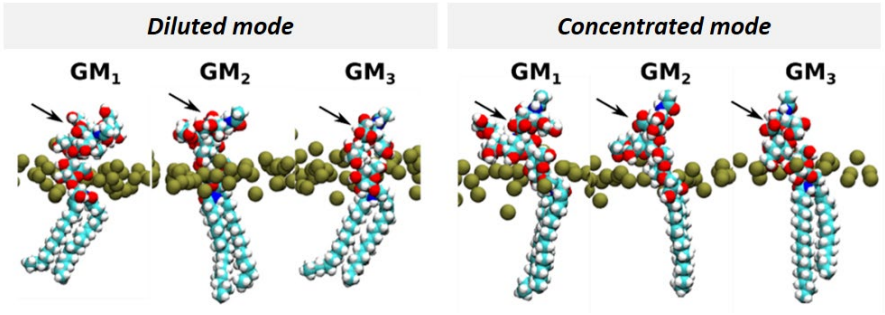

Figure 5.7 Representative structures of the most frequently sampled tilt angle of the glycan chain containing the sialic acid for each ganglioside in the diluted (no nanodomains) and concentrated (with nanodomains) modes. The arrow indicates the position of the sialic acid. The figure was taken from [56].

Table 5.3 Number of lipid molecules in each nanodomain (for both leaflets) calculated under the assumption that SM and GM_i gangliosides are exclusively localized in the nanodomains whereas DOPC is distributed equally in the whole bilayer. Both scenarios were assumed for Chol. The calculation is based on the results obtained from MC-FRET. All compositions included 4 mol% GM_i and 1 mol% total of the GM_i fluorescent analogue.

		Number of molecules in the domains				
	GM_i	**DOPC**	**SM**	**$Chol_{in}$**	**$Chol_{in\&out}$**	**GM_i**
DOPC *100*	GM_1	424	-	-	-	35
	GM_2	3127	-	-	-	270
	GM_3	3127	-	-	-	256
DOPC/SM *90/10*	GM_1	4124	975	-	-	487
	GM_2	43852	10367	-	-	5183
	GM_3	1318	232	-	-	116
DOPC/Chol *75/25*	GM_1	93550	-	62367	31183	12473
	GM_2	63673	-	45158	21224	9032
	GM_3	1878	-	1043	626	209
DOPC/Chol/SM *75/25/10*	GM_1	75762	21992	54980	29139	10996
	GM_2	66894	27083	67707	25729	13541
	GM_3	34255	11213	28032	13175	5606

5.1.4.2 Impact of ganglioside's backbone on the formation of nanodomains

From a mechanistic point of view, the properties and the extent of ganglioside lateral organization (i.e. formation of ganglioside domains) correlate with the length and degree of saturation of their acyl chains. [59–62] Naturally, gangliosides exhibit some degree of heterogeneity within their ceramide moiety, but typically miss double bonds in their saturated acyl chains. Based on the existing literature, it seems that the extent of ganglioside lateral segregation is modulated by differences in the saturation of acyl chains of gangliosides and the surrounding phospholipids, similarly as described for other sphingolipids.[63–65]

According to literature, the interactions between the backbone of the ganglioside and the surrounding suffice to induce formation of nanodomains. If all sugar units from a ganglioside are removed, the resulting ceramide (**Figure 5.5**) can self-segregate and form domains. For instance, ceramide has been shown to increase the size of pre-existing nanodomains in DOPC/SM/Chol (45.5/45.5/10) supported bilayers in a concentration-dependent manner.[66] Accordingly, the addition of 4 mol% ceramide to 1-palmitoyl-2-oleoyl-*sn*-glycero-3-phosphocholine (POPC)/SM/Chol vesicles resulted in the formation of highly ordered nanodomains with an estimated size of 4 nm and a bilayer coverage area of around 15%.[67] Similarly, SM (**Figure 5.5**) also undergoes nanoscopic segregation.[64] Nanodomains of 8 to 12 nm radius occupying 37–55% of the membrane area have been found in DOPC/SM (90-85/10-15) bilayers.[68] In ternary DOPC/Chol/SM (65/25/10) lipid mixtures, nanodomains of 9 nm in radius covering 45% of the bilayer area have been detected.[68]

In summary, although the ganglioside headgroup does not seem indispensable for the formation of sphingolipid nanodomains, it stabilizes the nanodomains and significantly influences their physicochemical features, including their size, fluidity and dynamics.[3]

*5.1.4.3 Modulation of ganglioside nanodomains by Cholera toxin (**PAPER VI** and **PAPER VII**)*

One of the functions of gangliosides in plasma membranes is to serve as receptors for various ligands. The nanoscale organization of gangliosides and its temporal regulation may be of pivotal importance in these membrane-associated processes. Nanodomain characteristics can modulate interactions with proteins, e.g., β-amyloid (Aβ) and pentameric bacterial toxins.[69–71] On the other hand the binding of lectins (proteins that recognize and bind to specific carbohydrates or larger

glycol structures without modifying them) can induce changes in the spatiotemporal features of the ganglioside nanodomains that are linked to functional effects.[72]

Over the years, the most studied ligand of gangliosides has been the pentavalent Cholera toxin B (CtxB) subunit, which has a strong affinity for GM_1.[53,73,74] We have shown that binding of CtxB significantly influences the biophysical properties of ganglioside nanodomains.[53] Specifically, binding of CtxB to GM_1 changes the phase state of the nanodomains from liquid-disordered (L_d) to liquid-ordered (L_o) and modulates their size and area coverage. In complex mixtures of DOPC/Chol/SM/(1,2-dioleoyl-sn-glycero-3-phospho-(1'-rac-glycerol), DOPG) (49/25/19/5) + 2 mol% GM_1 saturated by CtxB, CtxB binding reduces the average radius of nanodomains, from 26 nm to 8 nm, and their surface area coverage, from 30% to 6%.[53,71] These results thus demonstrate the very important and profound effects of CtxB binding to GM_1 on the properties of the GM_1 nanodomains. At the same time, as shown in [75], the presence of ganglioside nanodomains and the content of GM_1 in the lipid bilayer influences binding of CTxB. While at low GM_1 contents cholesterol reduces the recognition activity of GM_1 (most likely due to the suggested tilted conformation which is not suitable for binding), at higher GM1 densities (~4 %) cholesterol does not have any impact on GM_1- ligand interaction.

5.1.5 Inter-leaflet coupling of lipid nanodomains – insights by MC-FRET (PAPER VIII AND PAPER IX)

Thanks to the energy transfer that occurs not only within one bilayer leaflet but also from one leaflet to the other one (**Figure 4.2**), the measured FRET efficiency will also depend on the mutual organisation of the nanodomains in the lower and upper leaflets.[76] Thus, MC-FRET, in contrast to other fluorescence approaches, offers excellent axial resolution and can be used to study inter-leaflet organisation of nanodomains.[76,77] In principle, the following scenarios may arise (**Figure 5.8**): 1) Nanodomains are perfectly registered across the bilayer leaflets (**Figure 5.8A**), 2) the nanodomains in the upper and lower leaflets are independent from each other (**Figure 5.8B**) and 3) nanodomains are anti-registered (**Figure 5.8C**). In this case, the nanodomains in the two leaflets avoid each other, and thus, the nanodomains in the upper leaflet cannot occupy the lateral positions that have already been taken by the nanodomains in the lower leaflet, and vice versa. To identify the most likely scenario, the experimental time-resolved fluorescence decays of the donors in the presence of acceptors are fitted by the decays generated for the scenarios 1-3. As the most probable

is classified the scenario that provides the best fit and the lowest value of the chi2 parameter. Since the ability of MC-FRET to identify the most probable coupling scenario depends significantly on the extent to which the decays for scenarios 1, 2 and 3 differ, it can again be characterized by means of the parameter *RES*. The parameter is now defined as

$$RES = \frac{\sum_{i=1}^{n} abs(F_{\mathrm{DA,REG}}(t_i) - F_{\mathrm{DA,ANTI/INDEP}}(t_i))}{F_{\mathrm{DA,REG}}(t_i)n} \cdot 100 \quad (5.2)$$

Thus, *RES* expresses the difference between the time-resolved decay for the registered, $F_{\mathrm{DA,REG}}(t)$, and either the anti-registered, $F_{\mathrm{DA,REG}}(t)$, or independent, $F_{\mathrm{DA,REG}}(t)$, nanodomains.

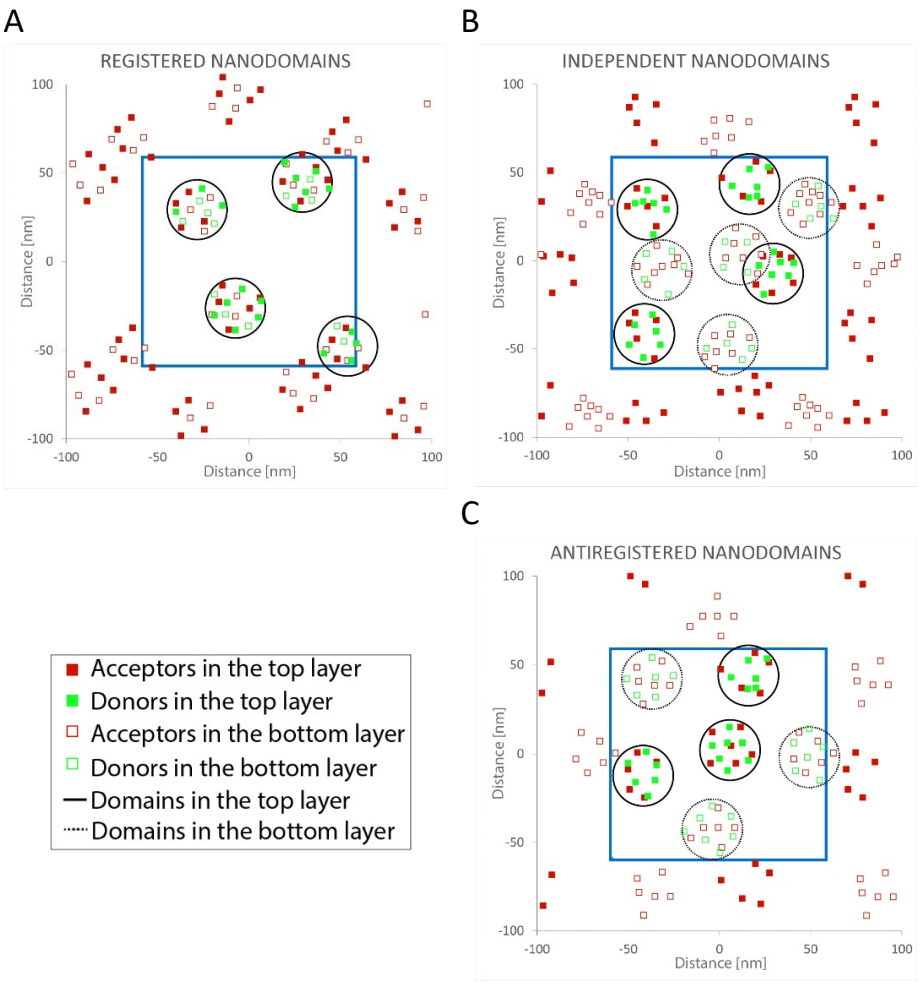

Figure 5.8 Schematic planar projection of the simulated lipid bilayer containing: A) perfectly registered; B) independent and C) antiregistered nanodomains. K_D (D), K_D (A) = 1000. The blue line indicates the boundaries of the basic simulation box. The figure was taken from [49].

As expected, the MC-FRET resolution improves, i.e. the *RES* values increase, as the probe affinity to one of the phases increases (**Figure 5.9**). Case II ($K_{\mathrm{D}}(\mathrm{D}) > 1$ and $K_{\mathrm{D}}(\mathrm{A}) < 1$) appears again to be the most robust one, exhibiting reasonable resolution for a wide range of $K_{\mathrm{D}}(\mathrm{D/A})$ values. Overall, the performed analysis identifies case I as the worst one, yielding at relatively high $K_{\mathrm{D}}(\mathrm{D/A}) = 10$ a relatively low $RES \leq 20$ followed by case III and case II. Nevertheless, even the least favourable case I can be used successfully.

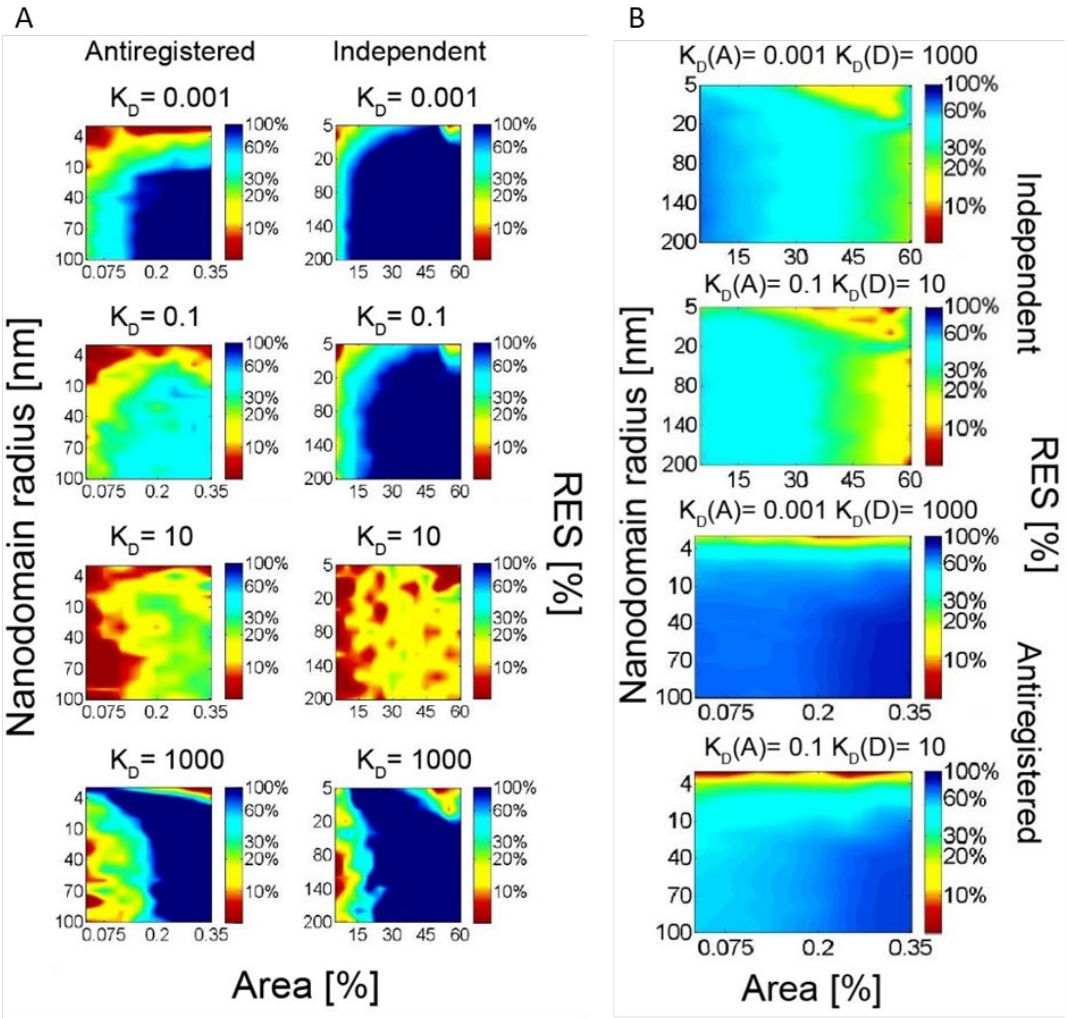

Figure 5.9 The potential of MC-FRET to resolve antiregistered/independent from registered nanodomains as a function of the nanodomain radius and the area occupied by the nanodomains. (A) K_{D} (D) = K_{D}(A), (B) K_{D} (D) ≥ 1 and K_{D} (A) ≤ 1. The figure was taken from [49].

In Vinklárek et al[77] we used headgroup-labelled gangliosides GM_1 ($K_D(D, A) \geq 20$) to provide the first experimental evidence that lipid nanodomains of the sizes between 10 and 160 nm formed at various lipid ratios of DOPC, Chol, SM and oxidized lipids (1-palmitoyl-2-(5′-oxo-valeroyl)-*sn*-glycero-3-phosphocholine (POVPC) and 1-palmitoyl-2-glutaryl-*sn*-glycero-3-phosphocholine (PGPC)) are inter-leaflet coupled. Recently, we used the same approach to show that GM_1, GM_2 and GM_3 ganglioside nanodomains ($\langle R \rangle \in \langle 7; 120 \rangle$ nm and $\langle A \rangle \in \langle 38; 61 \rangle$%), with the actual $\langle R \rangle$ and $\langle A \rangle$ parameters depending on the membrane lipid composition, are also inter-leaflet coupled.[56] Despite these few pieces of evidence, it remains largely unclear to what extent the registration of nanodomains is universal.[76]

5.1.6 Lipid diffusion in the presence of moving nanodomains (PAPER X)

Diffusion of lipids in a planar homogeneous bilayer follows a well-known diffusion law, which relates the mean square displacement (MSD) with time *t* and the diffusion coefficient *D* according to $\mathrm{MSD} = 4Dt$. A plot of MSD against *t* is referred to in literature as a "diffusion law plot". In analogy, by using FCS, a diffusion law plot can be constructed by plotting the square of the confocal waist w^2 (whose size can be modified) against the diffusion time τ_D. In membranes without obstacles, such a plot yields a straight line: $w^2 = 4D\tau_D$. In the presence of immobile nanodomains, the diffusion plots are strongly nonlinear and extrapolation of data towards shorter diffusion times yields a positive intercept on the τ_D axis, revealing anomalous sub-diffusion behaviour (**Figure 5.10**). [78–80] Thus, the nonlinearity of the diffusion law plots can be used to prove the presence of nanodomains in lipid bilayers. In [78] we questioned this frequently used microscopy approach. We simulated how lipid domain movement (up to now neglected) influences the diffusion time/spot-size dependence observed in FCS experiments and showed that domain movement substantially changes conclusions on 'anomalous' lipid diffusion in the presence of nanodomains, even when using super resolution methods. More specifically, as shown on **Figure 5.10**, the nonlinearity of diffusion plots quickly disappears when nanodomains are mobile. Additional components in the diffusion autocorrelation functions $G(\tau)$ are resolvable exclusively with confocal spots of sizes comparable to those of the moving nanodomains.[78] Thus, lipid probe movement will still appear as free diffusion in traditional confocal microscopy setups, with the existence of nanodomains possibly being reflected in a shift of the autocorrelation curves to longer

lag times (**Figure 5.10)**. Therefore, linear diffusion law plots without a positive intercept on τ_D axis do not directly exclude the presence of (mobile) nanodomains.[78]

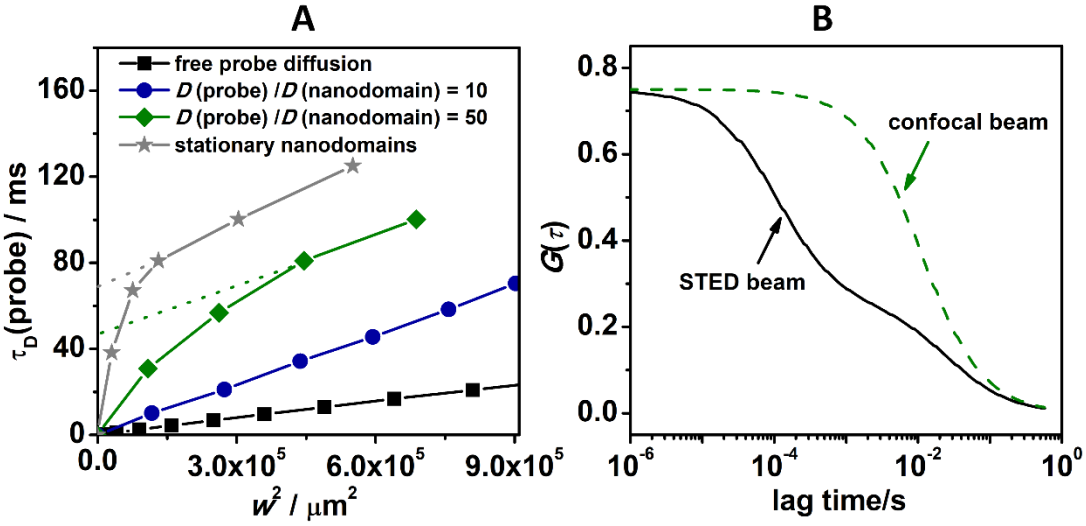

Figure 5.10 (A) A demonstrative diffusion law plot. This plot obeys a linear dependence in case of free diffusion on a planar lipid bilayer. The presence of nanodomains leads to a nonlinear shape of the plot with a positive intercept on the τ_D axis only if the nanodomain movement is slow in comparison to lipid probe diffusion. (B) An additional component in the FCS autocorrelation function appears only when the size of the focal spot is comparable to the size of the nanodomains and the partitioning of fluorescent probes into the nanodomains is strong. The figure was adopted from [78].

5.2 Relating protein oligomerization to membrane pore formation (**PAPER XI and PAPER XII**)

In-membrane oligomerization is decisive for the function (or dysfunction) of many proteins. Advances in single molecule and super-resolution fluorescence microscopy opened new possibilities to accurately determine in-membrane protein oligomerization numbers. However, the literature shows that these methods reveal broad distributions of oligomerization numbers for individually investigated membrane proteins.[81–84] This leads to the fundamental question, how one can identify functionally relevant oligomerization and distinguish it from unspecific aggregation. This question inspired us to develop a single molecule single vesicle statistical approach that

enables to determine the average oligomer size of a protein on a vesicle and verify its functionality - in this case membrane pore formation - at the same time.[85]

We introduced this approach on fibroblast growth factor 2 (FGF2), a protein that binds the plasma membrane by means of phosphatidylinositol 2 (PIP2) molecules where it subsequently oligomerizes into pores being a prerequisite for unconventional secretion of FGF2 into the extracellular space (**Figure 5.11**).[8,86,87]

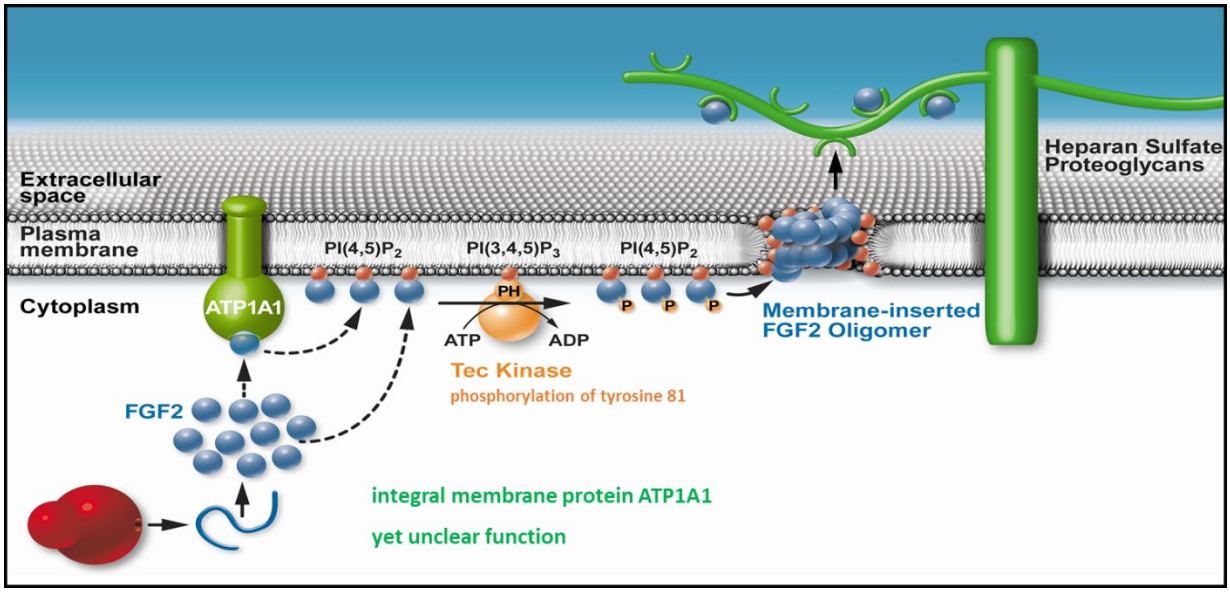

Figure 5.11 Protein FGF2, fulfilling its various biological functions in the extracellular space, is synthesized inside a cell and secreted into the extracellular space by a so-called unconventional secretion pathway, i.e. without the involvement of transporting vesicles. The translocation is initiated by binding of FGF2 to PIP2 lipids in the membrane. In the next step, the protein oligomerizes. The oligomerization is accompanied by opening of trans-membrane pores and subsequent release of the protein by means of heparan sulfate proteoglycans. The figure was taken from [88].

5.2.1 Principle of dual(+1)-FCS

The fluorescence assay applied to an ensemble of GUVs is essentially a dual-color fluorescence correlation spectroscopy (dual-FCS) assay with a third excitation-emission channel, called hereafter dual(+1)-FCS, that yields following relevant read-out parameters at the same time: 1) permeability of the membrane, which is directly related to membrane pore formation, 2) in-

membrane oligomeric size of FGF2-GFP expressed as the number of monomeric units per oligomer (N(m.u.)), 3) in-membrane diffusion coefficient of FGF2 (D(FGF2-GFP)) and 4) membrane surface concentration of FGF2 (c_{surf}(FGF2-GFP)). Thus, using this statistical approach, in-membrane oligomerization of FGF2 and formation of functional in-membrane pores can be linked to each other in one experiment at conditions close to physiological ones. The work-flow of the method is as follows (**Figure 5.12**):

A GUV is selected and classified as a leaky, i.e. containing membrane pores, or nonleaky one, i.e. containing an intact membrane, by means of Alexa-Fluor-532 (excitation 532 nm). Leaky GUVs are defined as GUVs filled by Alexa-Fluor-532 by more than 20%; similarly, nonleaky GUVs must be filled by less than 20%. In the next step, a membrane is placed into the waist of 470 and 635 nm lasers and a set of 60-second-long dual-color FCS measurements of membrane bound FGF2-GFP (excitation at 470 nm) and lipid tracer DOPE-Atto-633 (excitation at 635 nm) is performed. Whereas the blue fluorescence channel (excitation at 470 nm) is used to quantify c_{surf}(FGF2-GFP), D(FGF2-GFP) and N(m.u.)[FGF2-GFP], the red channel (excitation at 630 nm) is used for: visualization of all GUVs (including those without bound protein), correct vertical positioning of the membrane into the beam center as well as quality check of the membrane by measuring D(DOPE-Atto-633) and comparing this value to a-priori known D(DOPE-Atto-633).[89]

The obtained auto-correlation (AC) curves are fitted by a model assuming two-dimensional diffusion in the membrane (bound FGF2-GFP and DOPE-Atto-633), free three-dimensional diffusion in the solution (FGF2-GFP in the bulk) and transition of the dye to the triplet state:[90]

$$G(\tau) = 1 + \left(\frac{1}{N} \frac{1}{1+\left(\frac{\tau}{\tau_{\mathrm{D}}}\right)} + \frac{1}{N_{\mathrm{free}}} \frac{1}{1+\left(\frac{\tau}{\tau_{\mathrm{D,free}}}\right)\sqrt{1+\mathrm{SP}\frac{\tau}{\tau_{\mathrm{D,free}}}}} \right) \frac{1-T+T\exp\left(-\frac{\tau}{\tau_{\mathrm{T}}}\right)}{1-T} . \quad (5.3)$$

Here, N and N_{free} are the number of membrane-bound and free dye molecules in the confocal volume, τ_{D} and $\tau_{\mathrm{D,free}}$ the diffusion times of membrane bound and membrane free dye, SP the structure parameter, T the fraction of the dye in the triplet state and τ_{T} the lifetime of the triplet state. In the beam center, the fluorescent signal coming from the solution is negligible. This simplifies the above equation to

$$G(\tau) = 1 + \frac{1}{N} \frac{1}{1+\left(\frac{\tau}{\tau_{\mathrm{D}}}\right)} \frac{1-T+T\exp\left(-\frac{\tau}{\tau_{\mathrm{T}}}\right)}{1-T}. \quad (5.4)$$

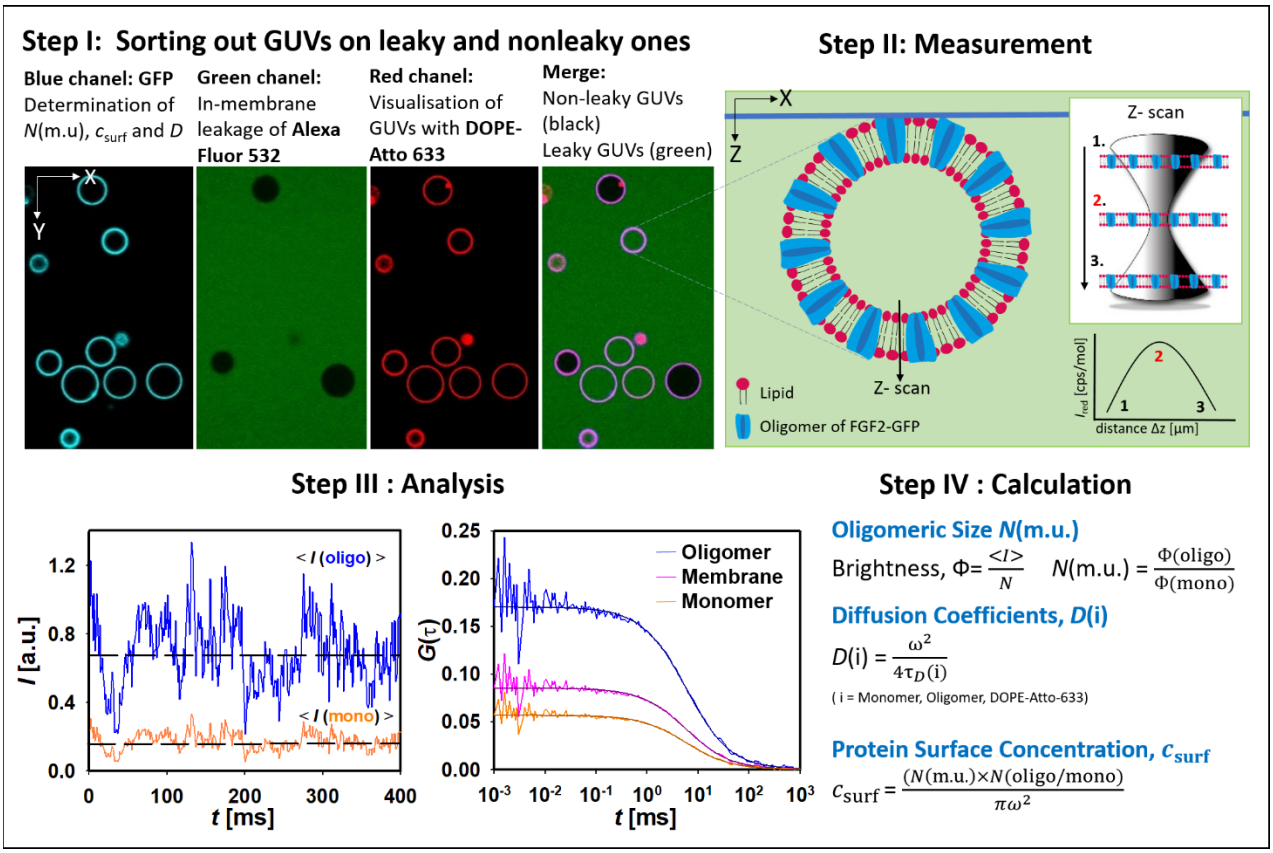

Figure 5.12 Workflow of dual(+1)-FCS: Step I) Sorting out GUVs into leaky and non-leaky ones by means of in-membrane leakage of Alexa-Fluor-532; Step II) Dual-color FCS on single GUVs. The measurement starts by focusing the bilayer into the beam center. This is achieved by finding the maximum in the red signal along the black arrow in the vertical XZ GUV plane. The correct membrane position is marked as '2'; Step III) The analysis that includes calculation of the average intensity for the monomer <*I*(mono)> and the oligomer <*I*(oligo)> and fitting the autocorrelation functions $G(\tau)$ for the monomer, oligomer and the lipid tracer DOPE-Atto-633. The fits yield the following output parameters: number of individually diffusing oligomers/monomers *N*(oligo/mono) in the confocal spot, and their corresponding diffusion times τ_D(oligo)/τ_D(mono); Step IV) Calculation of the final readout parameters. The figure was taken from [85].

The brightness of an oligomer is calculated as $\phi(\text{oligo}) = \frac{\langle I(\text{oligo})\rangle}{N}$, with $\langle I(\text{oligo})\rangle$ denoting the average fluorescence intensity of the oligomer. The brightness of a monomer $\phi(\text{mono})$ is obtained in a similar manner as $\phi(\text{oligo})$, but it needs to be ensured that the probability that two

labelled FGF2-GFP molecules meet in a cluster is negligible. Finally, the average oligomeric state can be calculated as

$$N(\text{m.u.}) = \frac{\phi(\text{oligo})}{\phi(\text{mono})}. \qquad (5.5)$$

and the protein surface concentration as the number of protein molecules in the confocal spot N(oligo/mono)*N(m.u.) of a known radius ω:

$$c_{\text{surf}} = \frac{N(\text{m.u.})N(\text{oligo/mono})}{\pi\omega^2}. \qquad (5.6)$$

5.2.2 Correlating FGF2 oligomeric state to membrane pore formation in a static manner

As shown on **Figure 5.12** (panel Step I), despite FGF2 binds to the membrane of most GUVs, some GUVs become leaky (i.e. containing pores) and others stay non-leaky (i.e. without pores) within a 4 hours long incubation time. The obtained distribution of average oligomer sizes for the entire ensemble of 60 investigated GUVs is clearly bimodal with most densely populated values

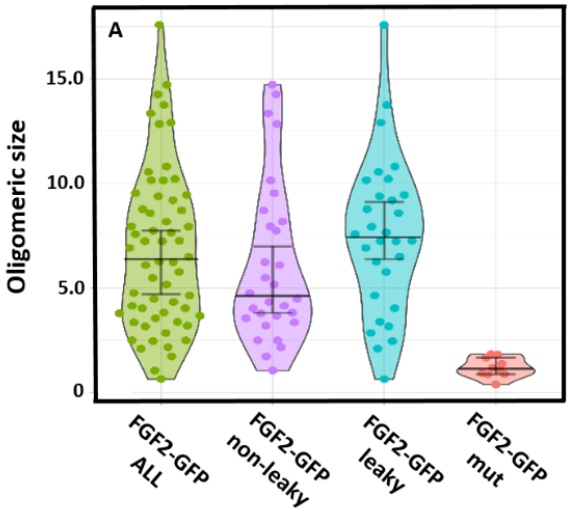

Figure 5.13: Functional correlation of (A) the oligomeric size (N(m.u.)) with membrane pore formation. Each dot corresponds to a data-point measured on single GUV. In the first step, all GUVs were taken for the analysis (FGF2-GFP ALL). In the next step, the GUVs were sorted out depending on membrane permeability into non-leaky (FGF2-GFP non-leaky) and leaky (FGF2-GFP leaky) ones. For comparison, the plots for double cysteine mutant His-FGF2-C77/95A-GFP where oligomerization is blocked are also shown (FGF2-GFP mut). Median values as well as 95% confidence intervals are indicated by the black solid lines. The figure was taken from [85].

around N(m.u.) ≈ 4 and N(m.u.) ≈ 8 (**Figure 5.13)**. By following in-membrane leakage of Alexa-Fluor-532, the GUVs can be sorted out into leaky and non-leaky ones. As shown on **Figure 5.13**, the determined oligomer size is significantly larger on leaky vesicles with a median value centered at median[N(m.u.)] = 7.4 in comparison to non-leaky ones with median[N(m.u.)] = 4.6. Correlation of the oligomeric size to membrane permeability thus identifies two distinct populations of FGF2-GFP differing in function that would otherwise not be revealed: the population of FGF2-GFP centered at median[N(m.u.)] = 7.4 that can permeabilize the membrane, and the other population centered at median[N(m.u.)] = 4.6 that lacks this ability. Importantly, a control experiment using a mutant of FGF2 where the oligomerization is blocked yields median[N(m.u.)] = 1.1.

5.2.3 Correlating FGF2 oligomeric state to membrane pore formation in a time-resolved manner

The same experiment can be performed in a time-resolved manner by measuring N(m.u.) on the same GUV during time. To demonstrate the principle of this approach, N(m.u.) was measured at the beginning (t = 0 hrs) when all GUVs where nonleaky and at the end of the incubation time ($t \geq 4$ hrs) (**Figure 5.14**). The presented data show that in 5 out of 8 cases, penetration of GUVs is accompanied by a significant increase in N(m.u.): in average from N(m.u., GUV w/o pores at t = 0 hrs) = 3.2 ± 2.07 to N(m.u, GUV with pores at $t \geq 4$ hrs) = 7.4 ± 2.89. In contrast, 4 out of 8 vesicles that remained intact throughout the measurement showed an increase in N(m.u.) from (N(m.u., GUV w/o pores) = 1.7 ± 0.52 at t = 0 hrs) to only (N(m.u., GUV w/o pores at $t \geq 4$ hrs) = 3.1 ± 1.54). These final values are thus significantly lower than in the first case. The FCS-based approach also identifies single GUVs not following these trends: GUV nr. 6 leaks most likely non-specifically (non-specific leakage was determined on an ensemble of 162 GUVs to be 17.9 %) whereas GUVs nr.13 to 16 do not leak despite a high final N(m.u.), presumably due to non-functional protein aggregation at the membrane surface. Dual(+1)-FCS can thus be used to not only monitor changes in N(m.u.) on the same GUV during formation of pores but also help identify functional and non-functional in-membrane oligomers.

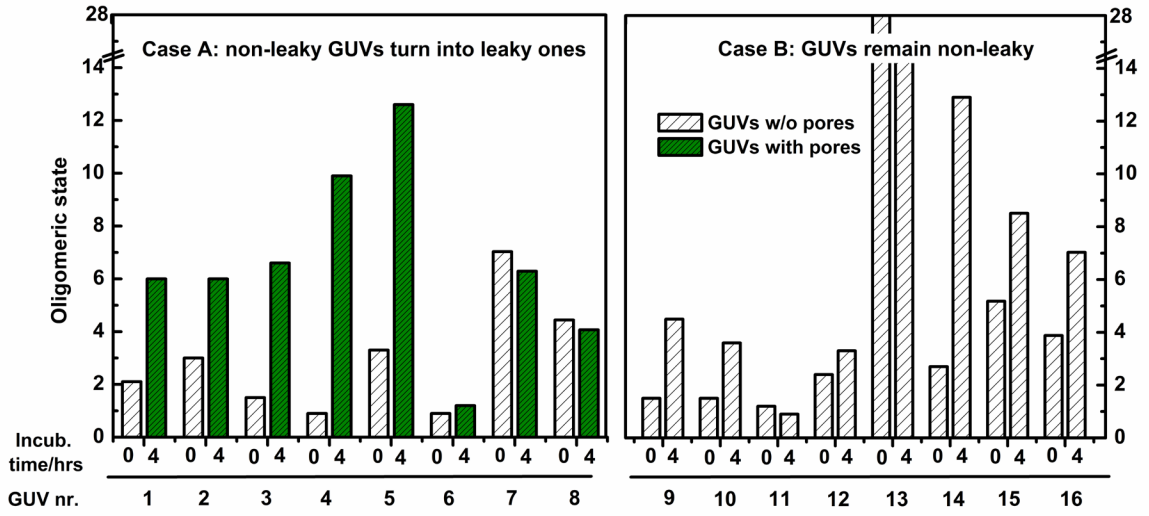

Figure 5.14 Correlation of the oligomeric size of FGF2-GFP and lipid pore formation in a time-resolved manner on single GUVs. GUVs that were not penetrated by the fluorescent tracer (GUVs w/o pores) at the start and got filled with the fluorescent tracer during incubation with FGF2-GFP (GUVs with pores) are shown in panel A. By contrast, GUVs that were not penetrated by the small fluorescent tracer throughout the time course of the experiment are shown in panel B. The figure was taken from [85].

5.3 Peptide dimerization as the driving force for membrane fusion (**PAPER XIII and PAPER XIV**)

Fusion of lipid membranes is a naturally occurring process in living cells. It is controlled by a coiled-coil interaction between complementary SNARE proteins.[9,11,91] Highly specific biological processes including fertilization, viral infection or controlled release of neurotransmitters are driven by membrane fusion. [11,91] It has recently attracted considerable scientific attention, not only for being essential for living organisms, but also for its potential to be used for *in vivo* applications such as drug delivery into cellular compartments. Despite a great importance of membrane fusion, it is still largely unclear how this process progresses at the nanoscale.

To uncover the initial steps of membrane fusion we have used single molecule FCS (fluorescence correlation spectroscopy), FCCS (fluorescence cross-correlation spectroscopy) and FRET (Förster resonance energy transfer). We mimicked the fusogenic activity of SNARE proteins by using a system based on two complementary lipopeptides CP_nE_4 and CP_nK_4

constructed from either a cationic peptide K_4 [(KIAALKE)$_4$] or anionic peptide E_4 [(EIAALEK)$_4$] coupled to a cholesterol membrane anchor via a flexible polyethylene glycol linker (**Figure 5.15**).[92–95] These lipopeptides were designed to fulfil all functional aspects of native membrane fusion.

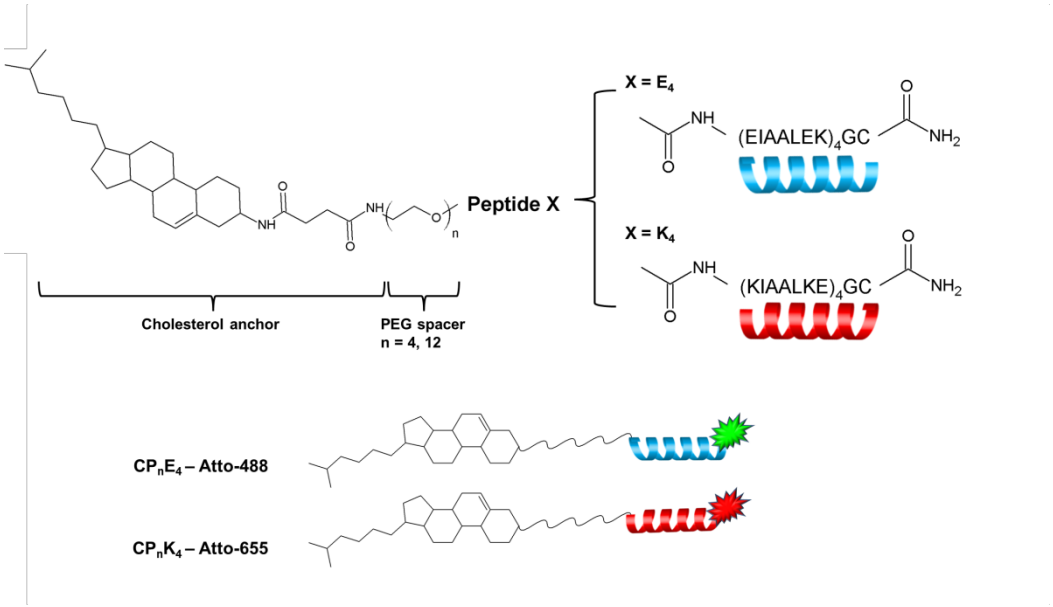

Figure 5.15. Chemical structures of CP_nE_4 and CP_nK_4 lipopeptides. A lipopeptide consists of a cholesterol moiety (C), a flexible poly(ethylene glycol) (PEG) linker of either 4 or 12 PEG units (P_4 or P_{12}) and one of the complementary peptides E or K. The lipopeptides were fluorescently labelled with either Atto-488 or Atto-655 at the C terminus of the peptide by a thiol-maleimide coupling.

Membrane fusion requires molecules to bring opposing membranes into close proximity, resulting in the local disturbance of the lipid bilayers in order to reduce the energetic costs of membrane fusion. The fusion process driven by CP_nE_4 and CP_nK_4 is based on coiled-coil formation between peptides E_4 and K_4. The formation of this coiled-coil is intended to mediate close contact of opposing membranes that the peptides are anchored in. The mechanistic details of lipopeptide mediated membrane fusion are as follows:[96]

1) CP_nK_4 and CP_nE_4 are localized at different distances from the lipid-water interface with a low chance of meeting/interacting with each other (**Figure 5.19**). The distance $d_{CPK\text{-}m}$ of Atto-488 attached to peptide K_4 in CP_nK_4 from the membrane was found, on average, 2.2 – 2.3 nm from

the lipid-water interface. The estimated maximal theoretical distances of Atto-488 from this plane that could be achieved were calculated to be 6.5 nm for CP_4K_4 and 9.3 nm for $CP_{12}K_4$, respectively. Comparison of these values with the measured distance suggests 'looping back' of the peptide segments in CP_4K_4 and $CP_{12}K_4$ to the lipid-water interface. Conversely, the distance $d_{CPE\text{-}m}$ of Atto-488 attached to CP_nE_4 from the bilayer surface equaled on average (6.7 ± 0.6) nm for CP_4E_4 nm or (6.0 ± 0.5) nm for $CP_{12}E_4$, respectively. This means that CP_nE_4 is in contrast to CP_nK_4 largely exposed to the bulk. Consequently, CP_nE_4 and CP_nK_4 cannot form hetero-coils with each other when reconstituted in the same bilayer. The efficiency of hetero-coiling is in fact so low that FCCS was not able to reveal any detectable amount of CP_4E_4-Atto-488/CP_4K_4-Atto-655 pairs. The different localization of the peptides along the bilayer normal may represent an important mechanism by which the number of free CP_nE_4 and CP_nK_4 molecules potentially available for binding to an opposing membrane is kept at a high level, enabling efficient fusion.

2) At the same time, both CP_nE_4 and CP_nK_4 are found in DOPC/DOPE/Chol (50/25/25 mol%) bilayers as monomers. Neither FCCS nor FRET experiments revealed any detectable amount of stable homo-oligomers in DOPC/DOPE/Chol (50/25/25 mol%) bilayers at a broad range of lipopeptide concentrations 0.05 -1.2 mol%. Such oligomers might potentially reduce the number of monomeric peptides which are available for binding to a complementary lipopeptide found in the approaching bilayer leaflet.
3) K_4, in contrast to E_4, interacts strongly with DOPC/DOPE/Chol (50/25/25 mol%) bilayers. Such strong binding is probably facilitated by the specific positioning of lysine residues and respective charge distribution within the primary sequence of peptide K_4.[23] Consequently, lipopeptides CP_nK_4 in contrast to CP_nE_4 exhibit an observable effect on DOPC/DOPE/Chol (50/25/25 mol%) bilayers (**Figure 5.20**). The peptide segments K_4 of CP_nK_4 molecules densely cover the surface of the bilayer at 2 mol% of CP_nK_4, which leads to increased microviscosity and decreased polarity of the carbonyl region of the lipid bilayer. In the past, dehydration has been shown to play an important role during membrane fusion.[46,47] At the same time, the diffusion of the lipid analogue DiD becomes impeded by 1 mol% of CP_nK_4 but not by CP_nE_4.

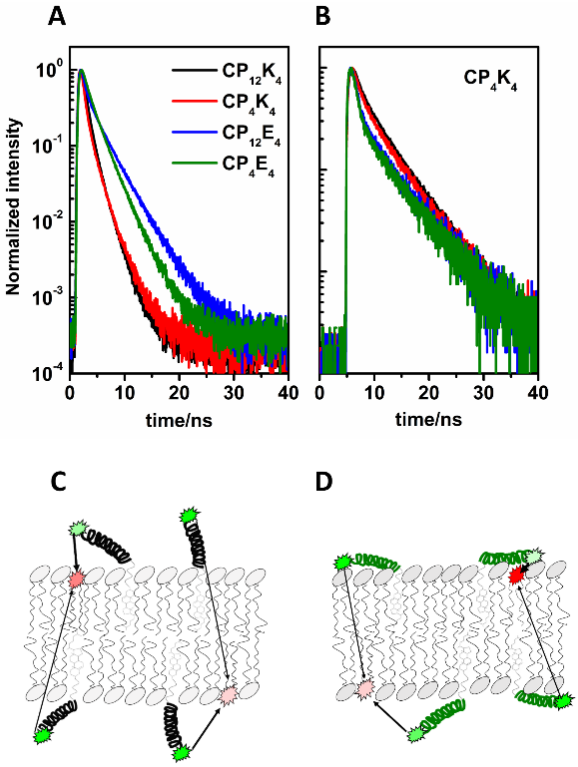

Figure 5.19 (A) Average normalized time-resolved fluorescence decays of CP_nE_4-Atto-488 and CP_nK_4-Atto-488 donors in the presence of DiD acceptors reporting on the distance of Atto-488 E and K peptides from the lipid-water interface. (B) An example of varying decays of CP_4K_4-Atto-488 in the presence of DiD obtained for a set of different GUVs. (C-D) Schematic pictures outlying the proposed orientations of CP_nK_4 (C) and CP_nE_4 (D) with respect to the lipid bilayer. The arrows point to the directions in which FRET can occur: within the same leaflet as well as across the lipid bilayer.

4) Surprisingly, binding of K_4 to E_4 is not efficient. According to single molecule cross-correlation FCS (FCCS) experiments (**Figure 5.21**), in which at the best 30% of the maximum cross-correlation amplitude was reached, the majority of CP_4E_4 and K_4 remain unbound to each other when up to a 10-fold excess of K_4 is added to CP_4E_4 containing GUVs. This occurs because K_4 sticks to the bilayer, where it diffuses with almost the same speed as the surrounding lipids. Similarly, significant amounts of CP_4K_4 and E_4 do not bind to each other when up to a 10-fold excess of E_4 is incubated with CP_4K_4 containing GUVs. This occurs because the equilibrium between free CP_4K_4 and E_4 and the resulting hetero-coil is shifted in

favour of the free components and is overwhelmed by interactions between CP_4K_4 and the lipid bilayer. E_4 behaves differently in comparison to K_4 in that it interacts with the bilayer exclusively by means of the complementary lipopeptide CP_nK_4.

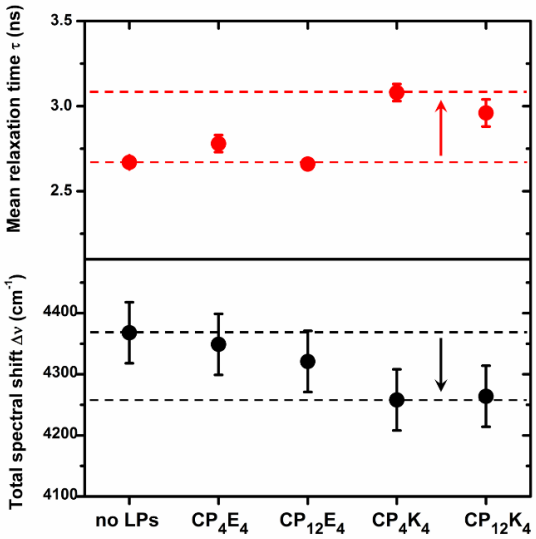

Figure 5.20 The solvent relaxation time τ_r and the spectral shift $\Delta\nu$ of Laurdan in DOPC/DOPE/Chol (50/25/25 mol%) LUVs containing 2 mol% of lipopeptides (LPs).

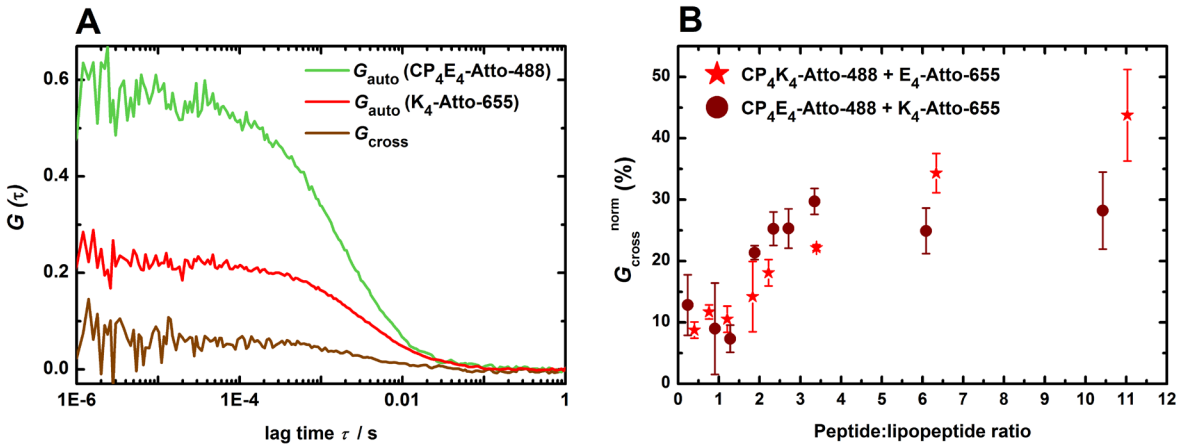

Figure 5.21 (Left): Representative auto-correlation functions G_{auto} for CP_4E_4-Atto-488 and K_4-Atto-655 obtained from an FCS measurement and the corresponding cross-correlation function (G_{cross}) obtained from a parallel FCCS measurement. (Right): The normalized cross-correlation amplitude, which reports on the extent of interaction between one of the peptides and the complementary lipopeptide, as a function of the peptide to lipopeptide ratio on DOPC/DOPE/Chol

(50/25/25 mol%) bilayers. The average value of $G_{\mathrm{cross}}^{\mathrm{norm}}$ was calculated based on measurements on at least 5 GUVs.

In conclusion, during the initial steps of membrane fusion, the main role of CP_nK_4 is to perturb the bilayer and poise it for undergoing fusion. On the other hand, CP_nE_4 molecules work as lipid anchors. The peptide moieties are exposed to the bulk, where they search for the complementary CP_nK_4 molecules, recruiting them to their own bilayer. All these facts represent important findings that need to be considered when a model for later stages of fusion is developed.

6. Conclusions

Recent advances in fluorescence microscopy and spectroscopy have enabled to characterize organisation of lipids and proteins in native plasma membranes with great spatiotemporal resolution. Although the biological implications are not clear yet, these experiments have shown that plasma membranes are nanoscopically heterogeneous in both its chemical composition and physical features.

In this habilitation work, a new high-resolution fluorescence method enabling characterization of biological membranes at the nanoscale has been successfully developed. This method, called MC-FRET, can (i) reliably detect nanoscopic heterogeneities formed in lipid bilayers, (ii) determine their sizes with the sensitivity down to only a few nanometres in radius, (iii) quantify their membrane surface coverage and (iv) characterize their mutual inter-leaflet organization. The limitations and possibilities of this method have been thoroughly characterized in **PAPER II** and **PAPER III**. This method has then been used to show that models of biological membranes containing two or more different types of lipids may be nanoscopically heterogenous. However, due to the extremely small size of these objects, they can hardly be considered as a newly formed phase. In my opinion, these results are important because they provide a clear proof for the nanoscopic heterogeneity of synthetic models of biological membranes that cannot be considered as homogeneous in their physicochemical features.

Furthermore, we used MC-FRET to elucidate the factors that drive nanoscopic segregation of gangliosides (which represent an important class of receptor lipids in the outer plasma membrane leaflet). Specifically, in **PAPER IV** and **PAPER V** it was concluded that the self-assembly of gangliosides is mainly controlled by their large oligosaccharide headgroup and hydrogen-bonding network formed both within and between the neighbouring headgroups. In **PAPER VI** and **PAPER VII**, it was also shown that the features of nanodomains are modulated by the interactions with pentameric Cholera toxin and vice versa that the ganglioside GM_1 to Cholera toxin interactions are modulated by the nanodomains. A few years later, in **PAPER VIII** and **PAPER IX**, the MC-FRET approach was upgraded to provide unique information about inter-leaflet organisation of the nanodomains. In this way, perfectly registered nanodomains have been detected in biological membranes for the first time. And finally, in **PAPER X,** the so called 'diffusion law' analysis of sv-FCS routinely used by fluorescence spectroscopists was revisited. We simulated how lipid domain movement (up to now neglected) influences the diffusion time/spot-size

dependence observed in FCS experiments and showed that domain movement substantially changes conclusions on 'anomalous' diffusion of nanodomains.

Furthermore, this thesis (**PAPER XI** and **PAPER XII**) introduces a new spectroscopic method called dual(+1)-FCS. It enables, by measuring the brightness of individually diffusing in-membrane oligomers, to determine simultaneously the average oligomeric state of a membrane-bound protein and membrane permeabilization of the investigated vesicle. In this way, membrane pore formation can be linked directly in on experiment with protein oligomerization in the membrane. Moreover, the assay allows for measuring the protein oligomeric state on the same lipid vesicle over time, enabling to capture changes in membrane permeabilization caused by protein oligomerization.

Finally, in the last two attached papers, i.e. in **PAPER XIII** and **PAPER XIV**, a molecular mechanism of membrane fusion inspired by SNARE proteins and based on two complementary lipopeptides CP_nE_4 and CP_nK_4 incorporated into the membrane by a cholesterol linker (C) has been investigated. A molecular evidence was provided that different distances of peptide E_4 in CP_nE_4 and peptide K_4 in CP_nK_4 from the bilayer represent an important mechanism, which enables fusion. Whereas E_4 is exposed to the bulk and solely promotes membrane binding of CP_nK_4, K_4 loops back to the lipid-water interface where it fulfils two distinct roles: it initiates bilayer contact by binding to CP_nE_4 containing bilayers; and it initiates fusion by modulating the bilayer properties.

In conclusion, in the framework of this habilitation thesis, two methods of fluorescence microscopy have been introduced and used in the research of membrane organisation and function. Whereas MC-FRET reaches a nanometre resolution in all three directions, dual(+1)-FCS combines measurements of in-membrane protein oligomerization with membrane permeabilization in a unique way. Both methods thus offer a powerful tool in the field of membrane biophysics.

7. References

1. Bernardino de la Serna, J., Schütz, G. J., Eggeling, C. & Cebecauer, M. There Is No Simple Model of the Plasma Membrane Organization. *Front. Cell Dev. Biol.* **4**, 1–17 (2016).
2. Cebecauer, M. *et al.* Membrane Lipid Nanodomains. *Chem. Rev.* **118**, 11259–11297 (2018).
3. Koukalová, A. *et al.* Lipid Driven Nanodomains in Giant Lipid Vesicles are Fluid and Disordered. *Sci. Rep.* **7**, 5460 (2017).
4. Sarmento, M. J., Ricardo, J. C., Amaro, M. & Šachl, R. Organisation of Gangliosides into Membrane Nanodomains. *FEBS Lett.* 1–30 (2020). doi:10.1002/1873-3468.13871
5. Shi, J. *et al.* GM1 clustering inhibits cholera toxin binding in supported phospholipid membranes. *J. Am. Chem. Soc.* **129**, 5954–5961 (2007).
6. Akl, M. R. *et al.* Molecular and clinical significance of fibroblast growth factor 2 (FGF2/bFGF) in malignancies of solid and hematological cancers for personalized therapies. *Oncotarget* **7**, 44735–44762 (2016).
7. Bikfalvi, A., Klein, S., Pintucci, G. & Rifkin, D. B. Biological roles of fibroblast growth factor-2. *Endocr. Rev.* **18**, 26–45 (1997).
8. Steringer, J. P. *et al.* Key steps in unconventional secretion of fibroblast growth factor 2 reconstituted with purified components. *Elife* **6**, 1–36 (2017).
9. Chen, Y. A. & Scheller, R. H. SNARE-mediated membrane fusion. *Nat. Rev. Mol. Cell Biol.* **2**, 98–106 (2001).
10. Jahn, R., Lang, T. & Südhof, T. C. Membrane fusion. *Cell* **112**, 519–533 (2003).
11. Martens, S. & McMahon, H. T. Mechanisms of membrane fusion: disparate players and common principles. *Nat. Rev. Mol. Cell Biol.* **9**, 543–56 (2008).
12. Betzig, E. *et al.* Imaging intracellular fluorescent proteins at nanometer resolution. *Science (80-.).* **313**, 1642–1645 (2006).
13. Rust, M. J., Bates, M. & Zhuang, X. Sub-diffraction-limit imaging by stochastic optical reconstruction microscopy (STORM). *Nat. Methods* **3**, 793–795 (2006).
14. Hell, S. W. & Wichmann, J. Breaking the diffraction resolution limit by stimulated emission: stimulated-emission-depletion fluorescence microscopy. *Opt. Lett.* **19**, 780 (1994).
15. Piliarik, M. & Sandoghdar, V. Direct optical sensing of single unlabelled proteins and super-resolution imaging of their binding sites. *Nat. Commun.* **5**, 1–8 (2014).
16. Young, G. *et al.* Quantitative mass imaging of single biological macromolecules. *Science (80-.).* **360**, 423–427 (2018).
17. Fujimoto, T. & Parmryd, I. Interleaflet Coupling, Pinning, and Leaflet Asymmetry—Major Players in Plasma Membrane Nanodomain Formation. *Front. Cell Dev. Biol.* **4**, 1–12 (2017).
18. *The Giant Vesicle Book*. (CRC Press, 2020).
19. Przybylo, M. *et al.* Lipid diffusion in giant unilamellar vesicles is more than 2 times faster than in supported phospholipid bilayers under identical conditions. *Langmuir* **22**, 9096–9099 (2006).
20. Eggeling, C. *et al.* Direct observation of the nanoscale dynamics of membrane lipids in a living cell. *Nature* **457**, 1159-U121 (2009).
21. Moertelmaier, M., Brameshuber, M., Linimeier, M., Schütz, G. J. & Stockinger, H. Thinning out clusters while conserving stoichiometry of labeling. *Appl. Phys. Lett.* **87**, 263903 (2005).
22. Roder, F. *et al.* Reconstitution of membrane proteins into polymer-supported membranes for probing diffusion and interactions by single molecule techniques. *Anal. Chem.* **83**, 6792–6799 (2011).
23. Tanaka, M. & Sackmann, E. Polymer-supported membranes as models of the cell surface. *Nature* **437**, 656–663 (2005).
24. Pace, H. *et al.* Preserved Transmembrane Protein Mobility in Polymer-Supported Lipid Bilayers Derived from Cell Membranes. *Anal. Chem.* **87**, 9194–9203 (2015).
25. Andersson, J. & Köper, I. Tethered and polymer supported bilayer lipid membranes: Structure and

function. *Membranes (Basel).* **6**, (2016).
26. Andersson, J., Köper, I. & Knoll, W. Tethered membrane architectures—design and applications. *Front. Mater.* **5**, 1–11 (2018).
27. Amaro, M. *et al.* Time-Resolved Fluorescence in Lipid Bilayers: Selected Applications and Advantages over Steady State. *Biophys. J.* **107**, 2751–2760 (2014).
28. Valeur, B. *Molecular Fluorescence Principles and Applications*. (Wiley-VCH Verlag GmbH, 2001). doi:10.1002/3527600248
29. Lakowicz, J. R. *Principles of fluorescence spectroscopy*. *Principles of Fluorescence Spectroscopy* (Springer, 2006). doi:10.1007/978-0-387-46312-4
30. Murphy, D. B. & Davidson, M. W. *Fundamentals of Light Microscopy and electronic Imaging*. (Wiley, 2013).
31. Van der Meer, B. . W., Coker, G. & Chen, S.-Y. . S. *Resonance Energy Transfer: Theory and Data*. (Wiley, 1994).
32. Förster, T. Zwischenmolekuläre Enegiewanderung und Fluoreszenz. *Ann. Phys.* **21**, 55–75 (1948).
33. Baumann, J. & Fayer, M. D. Excitation Transfer in Disordered Two-Dimensional and Anisotropic 3-Dimensional Systems - Effects of Spatial Geometry on Time-Resolved Observables. *J. Chem. Phys.* **85**, 4087–4107 (1986).
34. Šachl, R., Boldyrev, I. & Johansson, L. B. A. Localisation of BODIPY-labelled phosphatidylcholines in lipid bilayers. *Phys. Chem. Chem. Phys.* **12**, 6027–6034 (2010).
35. Schwille, P. & Haustein, E. Fluorescence correlation spectroscopy. An introduction to its concepts and applications. *Doi:10.1002/Lpor.200910041* 1–33 (2001). doi:10.1146/annurev.biophys.36.040306.132612
36. Ries, J., Petrášek, Z., García-Sáez, A. J. & Schwille, P. A comprehensive framework for fluorescence cross-correlation spectroscopy. *New J. Phys.* **12**, (2010).
37. Petrov, E. P. & Schwille, P. State of the art and novel trends in fluorescence correlation spectroscopy. *…and Qual. Assur. Fluoresc. …* 145–197 (2008). doi:10.1007/4243
38. Benda, A. *et al.* How to determine diffusion coefficients in planar phospholipid systems by confocal fluorescence correlation spectroscopy. *Langmuir* **19**, 4120–4126 (2003).
39. Smith, A. K. & Freed, J. H. Determination of Tie-Line Fields for Coexisting Lipid Phases: An ESR Study. *J. Phys. Chem. B* **113**, 3957–3971 (2009).
40. Farkas, E. R. & Webb, W. W. Precise and millidegree stable temperature control for fluorescence imaging: Application to phase transitions in lipid membranes. *Rev. Sci. Instrum.* **81**, (2010).
41. Ohvo-Rekilä, H., Ramstedt, B., Leppimäki, P. & Peter Slotte, J. Cholesterol interactions with phospholipids in membranes. *Prog. Lipid Res.* **41**, 66–97 (2002).
42. Silvius, J. R., Del Giudice, D. & Lafleur, M. Cholesterol at different bilayer concentrations can promote or antagonize lateral segregation of phospholipids of differing acyl chain length. *Biochemistry* **35**, 15198–15208 (1996).
43. Slotte, J. P. Sphingomyelin-cholesterol interactions in biological and model membranes. *Chem. Phys. Lipids* **102**, 13–27 (1999).
44. Boggs, J. M. Lipid intermolecular hydrogen bonding: influence on structural organization and membrane function. *Biochim. Biophys. Acta - Rev. Biomembr.* **906**, 353–404 (1987).
45. Hyvonen, M. T. *et al.* Molecular dynamics simulation of sphingomyelin bilayer. *J. Phys. Chem. B* **107**, 9102–9108 (2003).
46. Baoukina, S., Mendez-Villuendas, E., Bennett, W. F. D. & Tieleman, D. P. Computer simulations of the phase separation in model membranes. *Faraday Discuss.* 63–75 (2013). doi:10.1039/c2fd20117h
47. Huang, J. & Feigenson, G. W. Monte Carlo simulation of lipid mixtures: finding phase separation. *Biophys. J.* **65**, 1788–1794 (1993).
48. De Almeida, R. F. M., Loura, L. M. S., Fedorov, A. & Prieto, M. Lipid rafts have different sizes depending on membrane composition: A time-resolved fluorescence resonance energy transfer study. *J. Mol. Biol.* **346**, 1109–1120 (2005).

49. *Fluorescence Microscopy and Spectroscopy in Biology*. (Springer).
50. Šachl, R., Humpolíčková, J., Štefl, M., Johansson, L. B.-Å. & Hof, M. Limitations of electronic energy transfer in the determination of lipid nanodomain sizes. *Biophys. J.* **101**, L60–L62 (2011).
51. Šachl, R. & Johansson, L. B.-Å. Heterogeneous Lipid Distributions in Membranes as Revealed by Electronic Energy Transfer. in *Reviews in Fluorescence 2015* (ed. Geddes, C. D.) 171–187 (2016). doi:10.1007/978-3-319-24609-3_7
52. Sonnino, S., Prinetti, A., Mauri, L., Chigorno, V. & Tettamanti, G. Dynamic and Structural Properties of Sphingolipids as Driving Forces for the Formation of Membrane Domains. *Chem. Rev.* **106**, 2111–2125 (2006).
53. Štefl, M. *et al.* Dynamics and size of cross-linking-induced lipid nanodomains in model membranes. *Biophys. J.* **102**, 2104–2113 (2012).
54. Šachl, R. *et al.* On multivalent receptor activity of GM1 in cholesterol containing membranes. *Biochimica et Biophysica Acta - Molecular Cell Research* (2014).
55. Sarmento, M. J., Coutinho, A., Fedorov, A., Prieto, M. & Fernandes, F. Ca2 + induces PI(4,5)P2 clusters on lipid bilayers at physiological PI(4,5)P2 and Ca2 + concentrations. *Biochim. Biophys. Acta - Biomembr.* **1838**, 822–830 (2014).
56. Sarmento, M. J. *et al.* The impact of the glycan headgroup on the nanoscopic segregation of gangliosides. *Biophys. Journal, under Rev.*
57. Amaro, M. *et al.* GM1 Ganglioside Inhibits b-amyloid Oligomerization Induced by Sphingomyelin. *Angew. Chemie* **55**, 9411–9415 (2016).
58. Cantù, L., Corti, M., Brocca, P. & Del Favero, E. Structural aspects of ganglioside-containing membranes. *Biochim. Biophys. Acta - Biomembr.* **1788**, 202–208 (2009).
59. Masserini, M., Palestini, P. & Freire, E. Influence of glycolipid oligosaccharide and long-chain base composition on the thermotropic properties of dipalmitoylphosphatidylcholine large unilamellar vesicles containing gangliosides. *Biochemistry* **28**, 5029–5034 (1989).
60. Masserini, M. & Freire, E. Thermotropic characterization of phosphatidylcholine vesicles containing ganglioside GM1 with homogeneous ceramide chain length. *Biochemistry* **25**, 1043–1049 (1986).
61. Masserini, M. *et al.* Interactions of proteins with ganglioside-enriched microdomains on the membrane: the lateral phase separation of molecular species of GD1a ganglioside, having homogeneous long-chain base composition, is recognized by Vibrio cholerae sialidase. *Biochemistry* **27**, 7973–7978 (1988).
62. Sonnino, S. & Prinetti, A. Membrane domains and the "lipid raft" concept. *Curr. Med. Chem.* **20**, 4–21 (2013).
63. Sonnino, S., Mauri, L., Chigorno, V. & Prinetti, A. Gangliosides as components of lipid membrane domains. *Glicobiology* **17**, 1–13 (2006).
64. Sonnino, S., Prinetti, A., Mauri, L., Chigorno, V. & Tettamanti, G. Dynamic and structural properties of sphingolipids as driving forces for the formation of membrane domains. *Chem. Rev.* **106**, 2111–2125 (2006).
65. Sonnino, S. *et al.* Gangliosides in membrane organization. in *Progress in Molecular Biology and Translational Science* **156**, 83–120 (Elsevier Inc., 2018).
66. Ira & Johnston, L. J. Sphingomyelinase generation of ceramide promotes clustering of nanoscale domains in supported bilayer membranes. *Biochim. Biophys. Acta - Biomembr.* **1778**, 185–197 (2008).
67. Silva, L. C., de Almeida, R. F. M., Castro, B. M., Fedorov, A. & Prieto, M. Ceramide-domain formation and collapse in lipid rafts: membrane reorganization by an apoptotic lipid. *Biophys. J.* **92**, 502–516 (2007).
68. Koukalová, A. *et al.* Lipid driven nanodomains in giant lipid vesicles are fluid and disordered. *Sci. Rep.* **7**, 5460 (2017).
69. Šachl, R. *et al.* On multivalent receptor activity of GM1 in cholesterol containing membranes. *Biochim. Biophys. Acta* **1853**, 850–7 (2015).

70. Shi, J. *et al.* GM 1 Clustering Inhibits Cholera Toxin Binding in Supported Phospholipid Membranes. *J. Am. Chem. Soc.* **129**, 5954–5961 (2007).
71. Amaro, M. *et al.* GM1 ganglioside inhibits β-amyloid oligomerization induced by sphingomyelin. *Angew. Chemie - Int. Ed.* **55**, 9411–9415 (2016).
72. Johannes, L., Parton, R. G., Bassereau, P. & Mayor, S. Building endocytic pits without clathrin. *Nat. Rev. Mol. Cell Biol.* **16**, 311–321 (2015).
73. van Zanten, T. S. *et al.* Direct mapping of nanoscale compositional connectivity on intact cell membranes. *Proc. Natl. Acad. Sci.* **107**, 15437–15442 (2010).
74. Hammond, A. T. *et al.* Crosslinking a lipid raft component triggers liquid ordered-liquid disordered phase separation in model plasma membranes. *Proc. Natl. Acad. Sci.* **102**, 6320–6325 (2005).
75. Šachl, R. *et al.* On multivalent receptor activity of GM1 in cholesterol containing membranes. *Biochim. Biophys. Acta* **1853**, 850–7 (2015).
76. Sarmento, M. J., Hof, M. & Šachl, R. Interleaflet coupling of lipid nanodomains – insights from in vitro systems. *Front. Cell Dev. Biol.* **8**, 284 (2020).
77. Vinklárek, I. S. *et al.* Experimental Evidence of the Existence of Interleaflet Coupled Nanodomains: An MC-FRET Study. *J. Phys. Chem. Lett.* **10**, 2024–2030 (2019).
78. Šachl, R., Bergstrand, J., Widengren, J. & Hof, M. Fluorescence correlation spectroscopy diffusion laws in the presence of moving nanodomains. *J. Phys.D Appl. Phys.* **49**, 114002 (11pp) (2016).
79. Wawrezinieck, L., Rigneault, H., Marguet, D. & Lenne, P. F. Fluorescence correlation spectroscopy diffusion laws to probe the submicron cell membrane organization. *Biophys. J.* **89**, 4029–4042 (2005).
80. Favard, C., Wenger, J., Lenne, P.-F. & Rigneault, H. FCS diffusion laws in two-phase lipid membranes: determination of domain mean size by experiments and Monte Carlo simulations. *Biophys. J.* **100**, 1242–51 (2011).
81. Kuwana, T. *et al.* Bid, Bax, and Lipids Cooperate to Form Supramolecular Openings in the Outer Mitochondrial Membrane. *Cell* **111**, 331–342 (2002).
82. Subburaj, Y. *et al.* Bax monomers form dimer units in the membrane that further self-assemble into multiple coexisting species. *Nat. Commun.* **6**, 1–11 (2015).
83. Antonsson, B., Montessuit, S., Sanchez, B. & Martinou, J.-C. Bax Is Present as a High Molecular Weight Oligomer/Complex in the Mitochondrial Membrane of Apoptotic Cells. *J. Biol. Chem.* **276**, 11615–11623 (2001).
84. Salvador-gallego, R. *et al.* Bax assembly into rings and arcs in apoptotic mitochondria is linked to membrane pores. 1–13 (2016). doi:10.15252/embj.201593384
85. Šachl, R. *et al.* Functional Assay to Correlate Protein Oligomerization States with Membrane Pore Formation. *Anal. Chem.* **92**, 14861–14866 (2020).
86. Temmerman, K. *et al.* A direct role for phosphatidylinositol-4,5-bisphosphate in unconventional secretion of fibroblast growth factor 2. *Traffic* **9**, 1204–1217 (2008).
87. Dimou, E. *et al.* Single event visualization of unconventional secretion of FGF2. *J. Cell Biol.* jcb.201802008 (2018). doi:10.1083/jcb.201802008
88. Steringer, J. P. & Nickel, W. The molecular mechanism underlying unconventional secretion of Fibroblast Growth Factor 2 from tumour cells. *Biol. Cell* **109**, 375–380 (2017).
89. Benda, A. *et al.* How to determine diffusion coefficients in planar phospholipid systems by confocal fluorescence correlation spectroscopy. *Langmuir* **19**, 4120–4126 (2003).
90. Widengren, J., Mets, Ü. & Rigler, R. Fluorescence Correlation Spectroscopy of Triplet States in Solution: A Theoretical and Experimental Study. *J.Phys.Chem.* **99**, 13368–13379 (1995).
91. Jahn, R. & Scheller, R. H. SNAREs - Engines for membrane fusion. *Nat. Rev. Mol. Cell Biol.* **7**, 631–643 (2006).
92. Robson Marsden, H., Korobko, A. V., Zheng, T., Voskuhl, J. & Kros, A. Controlled liposome fusion mediated by SNARE protein mimics. *Biomater. Sci.* **1**, 1046 (2013).

93. Versluis, F. *et al.* In Situ Modi fi cation of Plain Liposomes with Lipidated Coiled Coil Forming Peptides Induces Membrane Fusion. (2013).
94. Yang, J. *et al.* Drug delivery via cell membrane fusion using lipopeptide modified liposomes. *ACS Cent. Sci.* **2**, 621–630 (2016).
95. Kong, L., Askes, S. H. C., Bonnet, S., Kros, A. & Campbell, F. Temporal Control of Membrane Fusion through Photolabile PEGylation of Liposome Membranes. *Angew. Chemie - Int. Ed.* **55**, 1396–1400 (2016).
96. Koukalová, A. *et al.* Distinct roles of SNARE-mimicking lipopeptides during initial steps of membrane fusion. *Nanoscale* **4**, 19064–19073 (2018).

8. List of attached papers

Corresponding author marked by *.

I) Koukalová, A., Amaro, M., Aydogan, G., Gröbner, G., Williamson, P. T. F., Mikhalyov, I., Hof, M. and **Šachl, R.*** Lipid Driven Nanodomains in Giant Lipid Vesicles are Fluid and Disordered. *Scientific Reports*, 7(1), 5460 (2017).

II) **Šachl, R**., Johansson, L.B.-Å. and Hof*, M Forster Resonance Energy Transfer (FRET) between Heterogeneously Distributed Probes: Application to Lipid Nanodomains and Pores. *Int. J. Mol. Sci.* 13:16141-16156 (2012).

III) **Šachl, R.**, Humpolíčková, J., Štefl, M., Johansson, L.B.-Å, Hof, M.* Limitations of Energy Tranfer in the Determination of Lipid Nanodomain Sizes. *Biophys. J.* 101:L60-L62 (2011).

IV) Maria J. Sarmento, Michael C. Owen, Joana C. Ricardo, Barbora Chmelová, David Davidović, Ilya Mikhalyov, Natalia Gretskaya, Martin Hof, Mariana Amaro, Robert Vácha and **Radek Šachl*** The impact of the glycan headgroup on the nanoscopic segregation of gangliosides, under review in *Biophys. J.*

V) M. J. Sarmento, J. C. Ricardo, M. Amaro and **R. Šachl*** (2020). Organisation of Gangliosides into Membrane Nanodomains. *FEBS Lett.*, 2020, 1–30.

VI) Štefl, M., **Šachl, R.**, Humpolíčková, J.*, Cebecauer, M., Macháň R., Johansson, L.B.-Å, Hof, M. Dynamics and Size of Crosslinking-Induced Lipid Nanodomains in Model Membranes. *Biophys. J.* 102:2104-2113 (2012).

VII) **Šachl, R.**, Amaro, M, Aydogan, G, Koukalová, A, Mikhalyov, I.I., Boldyrev, I, Humpolíčková, J.* and Hof, M. On multivalent receptor activity of GM1 in cholesterol containing membranes. *BBA-Molecular Cell Research* 1853:850-857 (2015).

VIII) Vinklárek, IS, Vel'as, L, Riegerová, P., Skála, K, Mikhalyov, I, Gretskaya, N, Hof, M and **Šachl, R**.* *J. Phys. Chem. Lett.*, 10, 2024–2030 (2019).

IX) Sarmento, M. J., Hof, M., and **Šachl, R.*** (2020). Interleaflet coupling of lipid nanodomains – insights from in vitro systems. *Front. Cell Dev. Biol.* 8, 284. doi:10.3389/FCELL.2020.00284.

X) **Šachl, R**,* Bergstrand, J, Widengren, J and Hof, M. Fluorescence correlation spectroscopy diffusion laws in the presence of moving nanodomains *J. Phys.D Appl. Phys.* 49 (2016).

XI) **Šachl, R***.; Čujová, S.; Singh, V.; Riegerová, P.; Kapusta, P.; Müller, H.-M.; Steringer, J. P.; Hof, M.; Nickel, W. Functional Assay to Correlate Protein Oligomerization States with Membrane Pore Formation. *Anal. Chem.* **2020**, *92*, 14861–14866.

XII) Steringer, J. P., Lange, S., Čujová, S., **Šachl, R**., Poojari, C., Lolicato, F., … Nickel, W.* Key steps in unconventional secretion of fibroblast growth factor 2 reconstituted with purified components. *eLife*, 6 (2017).

XIII) Koukalová, A., Pokorná, Š., Boyle, A.L., Mora, N.L., Kros, A., Hof, R. and **Šachl, R.*** Distinct roles of SNARE-mimicking lipopeptides during initial steps of membrane fusion. *Nanoscale*, **4**, 19064–19073, (2018).

XIV) Mora, N. L., Boyle, A. L., Kolck, B. J. Van, Rossen, A., Pokorná, Š., Koukalová, A., **Šachl, R**, Hof, M* and Kros, A* (2020). Controlled Peptide-Mediated Vesicle Fusion Assessed by Simultaneous Dual-Colour Time- Lapsed Fluorescence Microscopy. *Sci. Rep.* 10, 1–13.

9. Attached papers